Remote Sensing of Environment 247 (2020) 111941

Contents lists available at ScienceDirect

Remote Sensing of Environment

journal homepage: www.elsevier.com/locate/rse

Disruptive influences of residual noise, network configuration and data gaps on InSAR-derived land motion rates using the SBAS technique

Luyen K. Bui*, W.E. Featherstone, M.S. Filmer

School of Earth and Planetary Sciences, Curtin University of Technology, GPO Box U1987, Perth, WA 6845, Australia

ARTICLE INFO

Keywords:
Small baseline radar interferometry (SBAS)
InSAR network configuration
Data gaps
Optimal network design
Redundancy number

ABSTRACT

The interferometric synthetic aperture radar (InSAR) small baseline subset (SBAS) technique can be applied to land with varying deformation magnitudes ranging from mm/yr to tens of cm/yr. SBAS defines a network of interferograms that is limited by temporal and spatial baseline thresholds that are often applied arbitrarily, or in apparently subjective ways in the literature. We use simulated SAR data to assess (1) the influence of residual noise and SBAS network configuration on InSAR-derived deformation rates, and (2) how the number of interferograms and data gaps in the time series may further impact the estimated rates. This leads us to an approach for defining a SBAS network based on geodetic reliability theory represented by the redundancy number (*r*-number). Simulated InSAR datasets are generated with three subsidence signals of linear rates plus sinusoidal annual amplitudes of −2 mm/yr plus 2 mm, −20 mm/yr plus 5 mm and −100 mm/yr plus 10 mm, contaminated by Gaussian residual noise bounded within [−2; +2] mm, [−5; +5] mm and [−10; +10] mm, corresponding to standard deviations of approximately 0.5 mm, 1.5 mm and 3.0 mm, respectively. The influence of data gaps is investigated through simulations with percentages of missing data ranging from 5% to 50% that are selected (1) randomly across the 4-year time series, and (2) for three-month windows to represent the northern winter season where snow cover may cause decorrelation. These simulations show that small deformation rates are most adversely affected by residual noise. In some extreme cases, the recovered trends can be contrary to the signal (i.e., indicating uplift when there is simulated subsidence). We demonstrate through simulations that the *r*-number can be used to pre-determine the reliability of SBAS network design, indicating the *r*-values between ~0.8 and ~0.9 are optimal. *r*-numbers less than ~0.3 can deliver erroneous rates in the presence of noise commensurate with the magnitude of deformation. Finally, the influence of data gaps is not as significant compared to other factors such as a change in the number of interferograms used, although the blocks of "winter" gaps in the SBAS network show a larger effect on the rates than gaps at random intervals across the simulated time series.

1. Introduction and motivation

Interferometric synthetic aperture radar (InSAR) has been demonstrated to be a powerful tool for measuring the Earth's land-surface deformation owing to its high spatial and temporal resolution, wide spatial coverage, and ability to acquire data remotely (e.g., Hooper, 2008). However, InSAR measurements are contaminated by various error and noise sources, such as those caused by digital elevation models (DEMs), atmospheric signal path delay, orbital errors (ramps), temporal decorrelation, and other noise sources (e.g., Lee et al., 2012; Murray et al., 2019). Multi-temporal InSAR (MT-InSAR) methods were proposed to reduce these error and noise sources (e.g., Hooper, 2008). These methods work by analyzing a network of multiple acquisitions to derive the deformation time series and thus deformation rate (e.g., Shanker et al., 2011).

MT-InSAR methods can be classified into two principal categories, comprising the persistent scatterer (PS) method (e.g., Ferretti et al., 2001; Hooper et al., 2007; Hooper et al., 2004) and the small baseline subset (SBAS) method (e.g., Berardino et al., 2002; Cavalié et al., 2007; Hetland et al., 2012; López-Quiroz et al., 2009; Lundgren et al., 2001; Schmidt and Bürgmann, 2003; Usai, 2003). SBAS is among the most commonly used methods that makes use of a network of interferograms from which temporal and perpendicular baselines are limited in time and length to reduce the effects of geometric decorrelation (e.g., Crosetto et al., 2016; Shanker et al., 2011; Zebker and Villasenor, 1992). This also incorporates an approach to connect multiple SBASs

* Corresponding author.
E-mail address: buikhacluyen@humg.edu.vn (L.K. Bui).

https://doi.org/10.1016/j.rse.2020.111941
Received 8 January 2020; Received in revised form 30 May 2020; Accepted 4 June 2020
Available online 19 June 2020

that results in an increase in temporal and spatial sampling (Berardino et al., 2002). The SBAS method has been used to measure land deformation of various magnitudes, ranging from mm/yr (e.g., Elliott et al., 2010; Furuya et al., 2007; Jiang et al., 2011; Schmidt and Bürgmann, 2003) to cm/yr (e.g., Amelung et al., 1999; Cavalié et al., 2013; Chaussard et al., 2014; Lee et al., 2012) or even tens of cm/yr (e.g., Chaussard et al., 2014; López-Quiroz et al., 2009; Motagh et al., 2007; Short et al., 2011).

InSAR data are degraded by various error and noise sources. The error caused by DEM uncertainty can be reduced by a number of methods correcting for interferograms (e.g., Berardino et al., 2002; Bombrun et al., 2009) or deformation time series (e.g., Fattahi and Amelung, 2013; Pepe et al., 2011). In order to reduce the effect of satellite orbital errors (ramps), polynomial models based on network-sense (Biggs et al., 2007; Cavalié et al., 2008; Jolivet et al., 2012; Lin et al., 2010) or GPS data (e.g., Neely et al., 2020; Tong et al., 2013) can be used. A number of methods can be applied to correct atmosphere phase errors utilizing the stacking method (e.g., Biggs et al., 2007; Tymofyeyeva and Fialko, 2015), using local data assimilation, e.g., local atmospheric data (e.g., Delacourt et al., 1998) or zenith total delay (ZTD) computed from GPS data (e.g., Williams et al., 1998; Yu et al., 2018a; Yu et al., 2017), utilizing global or regional atmospheric models (e.g., Doin et al., 2009; Jolivet et al., 2011), or integrating a global atmospheric model and GPS data to an atmospheric correction model (e.g., Yu et al., 2018b). Although these methods can be used to cope with different errors and noise in InSAR measurements, they cannot be conducted perfectly, which leads to remaining or residual errors and noise. Additionally, because of scheduling or other technical issues, SAR images are not always regularly captured, or in other cases, blocks of images acquired during extended periods (e.g., winter snowfall) may be omitted from processing due to very low coherence, both of which may have a detrimental influence on the estimated time series (e.g., Kim et al., 2015; Kohlhase et al., 2003).

In InSAR SBAS data processing, pairs of scenes are chosen to form interferograms from which an interferogram network is built in such a way to reduce decorrelation noise through minimizing their time spans, and differences in look angle and squint angle (Hooper et al., 2012). Coherent pixels to which a specific SBAS approach are applied can subsequently be selected based on specific criteria, e.g., amplitude dispersion, spatial coherence, spectral coherence or their combination (Crosetto et al., 2016). Different proposed SBAS approaches are therefore based on thresholds that are, to a lesser or greater extent, different depending on various factors, e.g., applications, data availability or the critical baseline, which in turn depends on the wavelength of the radar sensor, spatial resolution and incidence angle (Gatelli et al., 1994; Zebker and Villasenor, 1992).

The temporal baseline threshold has been chosen varying from months to years (e.g., Lanari et al., 2007; López-Quiroz et al., 2009), while the perpendicular baseline threshold has been chosen ranging between hundreds of meters and over one thousand meters (e.g., Berardino et al., 2002; Chaussard et al., 2014). The SBAS network thresholds are used with the aim of maximizing the number of InSAR interferograms while minimizing their temporal and spatial decorrelation, as well as reducing the computation time and data burden. Baseline thresholds and pixel selection criteria used in several main SBAS approaches are listed in Table 1. The question then arises as to whether there is some more objective means by which to select these thresholds, which we consider herein. In this study, we deal with thresholds used to select InSAR image pairs with an assumption that all pixels are of relatively high coherence so as to be considered for SBAS processing.

We also consider the configuration of the SBAS network during our simulations. The so-called network "optimization" problem has been applied to geodetic (surveying) networks, which is traditionally divided among zero-, first-, second- and third-order problems (e.g., Grafarend and Sansò, 1985). The zero-order design (ZOD) is adopted for designing a reference system, thus is also called "datum problem" (Teunissen, 1985). In the first-order design (FOD), a network configuration is adopted by choosing the "optimal" locations of points in a geodetic network that result in small changes in the positions of the preliminary chosen network points (Berné and Baselga, 2004; Koch, 1985). The objective of second-order design (SOD) is to select "optimal" weights for the sometimes-different observations in which three approaches can be utilized, including (*i*) direct approximation of the criterion matrix, (*ii*) iterative approximation of the criterion matrix, and (*iii*) direct approximation of the inverse criterion matrix (Schmitt, 1985a). By applying SOD, one seeks a network with high precision (Amiri-Simkooei, 2004). In the third-order design, an existing network is improved, extended or densified by introducing new points and/or additional measurements (Schmitt, 1985b). This is also called the densification problem and can be understood to be a mixture of FOD and SOD. A combined design, introduced by Vaníček and Krakiwsky (1986), refers to the case where FOD and SOD problems are solved simultaneously.

In the experiments presented here, we use a time series of simulated InSAR data for which we have control on the amount of error and residual noise introduced. We then investigate the following parameters to determine what effect they have on InSAR-derived rates of [simulated] land deformation. Our overarching aim is to find an "optimal" network of interferograms that results in reduced data processing time. We assess 1) the influence of residual errors and noise on SBAS-derived rates and the root mean square (RMS) of the difference between simulated and SBAS-derived deformation time series for different scenarios of the signal to noise ratio (SNR), 2) the effect of data gaps (i.e., missing scene acquisitions) for both random and the three-month "winter" cases, and 3) the use of redundancy numbers from geodetic network theory to design an "optimal" SBAS network.

2. InSAR SBAS algorithm used for this experiment

In summary, SBAS starts by forming an interferogram network using temporal and perpendicular baseline thresholds, followed by selecting coherent pixels in which noise is assumed to be negligible. Phase unwrapping is another step implemented in SBAS that can be carried out either before or after pixel selection, depending on the implementation strategy (Gong et al., 2016). The inversion step is subsequently implemented to convert small baseline interferograms phase differences to a time series of displacements at the acquisition times. With m interferograms generated from $(n + 1)$ InSAR images, the inversion equation can be written as (Berardino et al., 2002):

$$\boldsymbol{A}\boldsymbol{\phi} = \delta\boldsymbol{\phi} \tag{1}$$

where $\boldsymbol{A}$ is the design matrix of size $m \times n$, $\boldsymbol{\phi}$ is the vector of n (unknown) time series phase displacements of InSAR images at a pixel, $\boldsymbol{\delta\phi}$ is the vector of m (known) phase differences between each small baseline interferogram. In the SBAS approach applied in these simulations, the interferogram phase measurements can be expressed as (Agram et al., 2012; Gong et al., 2016):

$$\delta\phi_{ij} = \phi_j - \phi_i = \sum_{n=i}^{j-1} \delta\varphi_n \tag{2}$$

where $\delta\phi_{ij}$ is the interferogram phase connecting i^{th} and j^{th} images, ϕ_i and ϕ_j are the phase values at i^{th} and j^{th} acquisitions, respectively, $\delta\varphi_n$ is the pixel phase increment between n^{th} and $(n + 1)^{th}$ images. Eq. (2) is utilized with an assumption of linear deformation between acquisitions that are adjacent in time (Berardino et al., 2002).

In SBAS data processing, a network is formed by choosing interferometric pairs with short temporal and perpendicular baselines limited by user-prescribed thresholds, and this controls the structure of the design matrix $\boldsymbol{A}$ in Eq. (1). With the above assumption of $(n + 1)$ InSAR images, the possible number of interferometric pairs (m) satisfies (Berardino et al., 2002):

Table 1
Summary of the main SBAS approaches.

Reference	Interferogram selection thresholds	Pixel selection mmcriterion
Berardino et al. (2002)	Perpendicular baseline (130 m)	Coherence
Mora et al. (2003)	Perpendicular baseline (24 m)	Coherence
Schmidt and Bürgmann (2003)	Perpendicular baseline (200 m)	Coherence
Lanari et al. (2004)	Perpendicular baseline (130 m)	Coherence
Hooper (2008)	Perpendicular baseline Temporal baseline Doppler baseline	Amplitude and phase stability
López-Quiroz et al. (2009)	Perpendicular baseline (500 m) Temporal baseline (9 months)	Coherence
Goel and Adam (2014)	Perpendicular baseline (150 m) Temporal baseline (150 days)	Statistical homogeneity test

$$\frac{n+1}{2} \le m \le \frac{n(n+1)}{2} \tag{3}$$

For each pixel selected, Eq. (1) is applied to convert the phase difference from interferograms in the chosen network to the phase time series of displacements according to InSAR acquired times by applying least-squares (LS) (Schmidt and Bürgmann, 2003), singular value decomposition (SVD) (Berardino et al., 2002), or minimization of the L1-norm (Lauknes et al., 2011). In most SBAS approaches, the design matrix $\boldsymbol{A}$ is fixed to be used in the inversion step for all selected pixels. This is an advantage in terms of convenience and reduced processing time, but may suffer from decorrelation, particularly in vegetated or snow-covered areas where many pixels may decorrelate, so that there are large gaps in the spatial distribution of its products, e.g., a velocity map (Sowter et al., 2013). Methods using a flexible design matrix $\boldsymbol{A}$, e.g., the intermittent SBAS method (Sowter et al., 2013), have been proposed as a solution. In this simulation, however, we use a fixed-size $\boldsymbol{A}$ matrix.

3. Network design used in geodesy

Geodetic surveying network "optimization" aims at finding a geometric configuration and a set of observations of sufficient precision to satisfy the desired positional quality criteria with lower financial and logistical costs (e.g., Kuang, 1993). The quality of a geodetic network is defined by the criteria of precision, reliability and economy (i.e., cost) of the network (Schmitt, 1985a). In geodetic network design, one seeks to minimize the objective function of economy and/or maximize that of precision or reliability of the network (e.g., Amiri-Simkooei, 2004).

The observational precision and network geometry are two crucial factors that influence the precision of a geodetic network. The variance-covariance (VCV) matrix is normally adopted to represent the network's precision. With the assumption of a minimum constraint, the VCV matrix is expressed as (e.g., Kuang, 1996).

$$\boldsymbol{C}_x = \sigma_0^2 \left[(\boldsymbol{A}^T\boldsymbol{P}\boldsymbol{A} + \boldsymbol{D}\boldsymbol{D}^T)^{-1} - \boldsymbol{H}(\boldsymbol{H}^T\boldsymbol{D}\boldsymbol{D}^T\boldsymbol{H})^{-1}\boldsymbol{H}^T \right] \tag{4}$$

where ${\sigma_0}^2$ is the a priori variance factor, $\boldsymbol{A}$ and $\boldsymbol{P}$ are the design and weight matrices of observations, $\boldsymbol{D}$ and $\boldsymbol{H}$ are the minimum and inner constraint datum information matrices, respectively.

The reliability of geodetic networks, as defined classically by Baarda (1968), is the ability of a network to detect and resist against gross errors in observations. It is further divided into internal and external reliability as follows.

1) The internal reliability is defined as the ability of a network to detect gross errors, referring to the lower bounds of detectable gross errors (aka. The minimum detectable bias, MDB) that is expressed as (e.g., Baarda, 1968):

$$\nabla_0 l_i = \frac{\delta_0 \sigma_{l_i}}{\sqrt{r_i}} \tag{5}$$

where δ_0 is the lower bound for the non-centrality parameter, σ_{l_i} and r_i are the standard deviation and the redundancy or r-number of the i^{th} observation, respectively. The r-numbers of the observations are the diagonal elements of the matrix $\boldsymbol{R}$ that are expressed as (e.g., Amiri-Simkooei et al., 2012):

$$\boldsymbol{R} = \boldsymbol{I} - \boldsymbol{A}(\boldsymbol{A}^T\boldsymbol{P}\boldsymbol{A})^{-1}\boldsymbol{A}^T\boldsymbol{P} \tag{6}$$

where $\boldsymbol{I}$ is the identity matrix.

2) The external reliability refers to the maximum effect of an undetectable gross error ($\nabla_0 l_i$) on the estimates of unknown parameters as:

$$\nabla_{0,i}\hat{x} = (\boldsymbol{A}^T\boldsymbol{P}\boldsymbol{A})^{-1}\boldsymbol{A}^T\boldsymbol{P}\nabla_{0,i}\, l \tag{7}$$

The internal reliability criterion is generally used as the measure for an "optimal" design of geodetic networks aiming at high reliability (Amiri-Simkooei, 2001), as shown in Eq. (6). In this paper, we examine the redundancy number (r-number) as a diagnostic metric to determine the likely effectiveness of the SBAS network design and verify this with simulation experiments. Specifically, for a given SBAS network with a corresponding design matrix $\boldsymbol{A}$ as shown in Eq. (1), the r-number is computed using Eq. (6) with the weights $\boldsymbol{P}$ of interferograms computed as the inverse of normalized (perpendicular and temporal) baseline lengths, which will be described in Section 4.

4. Generation of simulated data

A time series of independent pixels that are reasonably representative of the range of Earth deformations detected by InSAR are simulated, these being: mm/yr (e.g., Elliott et al., 2010; Furuya et al., 2007; Jiang et al., 2011; Schmidt and Bürgmann, 2003), cm/yr (e.g., Amelung et al., 1999; Cavalié et al., 2013; Chaussard et al., 2014; Lee et al., 2012), and tens of cm/yr (e.g., Chaussard et al., 2014; López-Quiroz et al., 2009; Motagh et al., 2007; Short et al., 2011). Our simulated data cover a four-year time span with 11-day sampling interval that corresponds to 133 equally time-spaced InSAR images. The baseline history of these 133 images, which is defined as the perpendicular baselines between images and the reference one (i.e., the first scene), is assumed to be within $[-200, +200]$ m, which is approximately the order of modern SAR missions such as C-band Sentinel-1 (Yague-Martinez et al., 2016) or TerraSAR-X (TSX) (e.g., Chen et al., 2016; Lubitz et al., 2013). The simulated baseline history of 133 images is generated randomly with ranges between -200 m and $+200$ m with that of the first scene being fixed to be zero (so leaving 132), and are shown as a scatter plot in Fig. 1.

We take an interest in a land subsidence signal with both a linear trend and a superposed annual sinusoidal oscillation; all pixels are simulated to experience surface deformation in the SAR line of sight (LoS) with linear plus annual periodic terms, which are expressed as:

$$d_{i,j} = v_i t_j + a_i \sin(2\pi t_j) \tag{8}$$

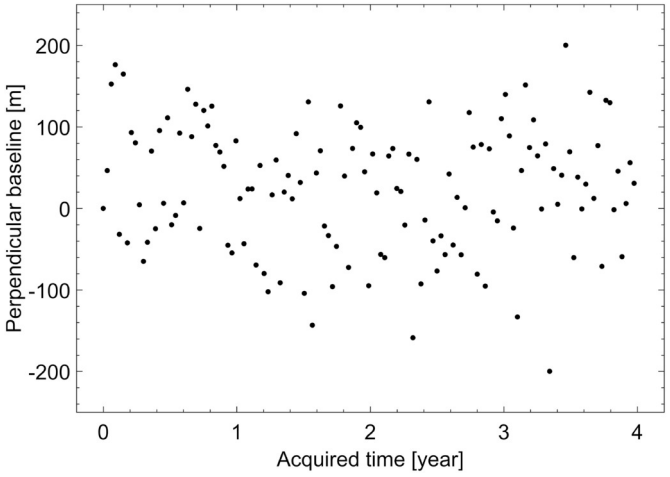

Fig. 1. Scatter plot of simulated perpendicular baseline history. Each black dot represents a SAR scene acquisition.

where $d_{i,\,j}$ is the deformation of the i^{th} pixel at the j^{th} image with corresponding acquired time t_j, v_i and a_i are the linear rate (velocity) and annual amplitude of the same pixel, respectively. We select this model form because time series analysis of other environmental phenomena do likewise (e.g., Davis et al., 2012; Didova et al., 2016).

The linear rates are chosen as −2 mm/year, −20 mm/year and −100 mm/year over the four-year period, which are representative of Earth deformation rates measured by InSAR (e.g., Cavalié et al., 2013; Chaussard et al., 2014; Elliott et al., 2010). The sinusoidal annual amplitude of Earth surface deformation has been drawn from the literature, which can range from the order of millimeters to centimeters (e.g., Baldi et al., 2009; Bock et al., 2012; Davis et al., 2012; Dzurisin et al., 2009; Murray and Lohman, 2018; Osmanoğlu et al., 2011). For example, Osmanoğlu et al. (2011) report annual amplitudes of GNSS stations ranging from several millimeters up to ~2.6 cm. Murray and Lohman (2018) found seasonal amplitudes up to ~5 cm in California detected by InSAR and peak-to-peak amplitudes of ~6 cm from GNSS in the Amazon Basin (cf. http://geodesy.unr.edu/NGLStationPages/stations/NAUS.sta).

While there can be large annual signals in various parts of the world, we simulate more conservative cases of simulated deformation signal with pairs of signal parameters of linear rate plus annual amplitudes that are shown in Table 2. We then apply a Monte Carlo simulation (e.g., Kroese et al., 2014) with 1000 pixels for each scenario. The number of tested pixels is chosen to avoid prohibitive computation times for the simulation experiments. The deformation time series of the 1000 pixels are then computed for the 133 equally spaced 11-day acquisition times using Eq. (8), and are termed herein the "simulated deformation time series". These are considered to be the "true" or noise-free signal, and will be used to validate the SBAS InSAR data processing results later in this paper.

With 133 InSAR images, the maximum possible number of interferograms is 8778 (Eq. (3)). These 8778 noise-free interferograms are then computed based on this simulated deformation SAR time series: the phase difference of an interferogram connecting i^{th} and j^{th} images is computed by subtracting the simulated time series value at i^{th} time from that at j^{th} time.

Table 2
The three cases of simulated signals showing linear rates and annual amplitudes used for experiments in Sections 5–7.

Signal case	Linear rate [mm/yr]	Annual amplitude [mm]
1	−2	2
2	−20	5
3	−100	10

Table 3
Simulated noise with various ranges and standard deviations.

Noise case	Range [mm]	Standard deviation [mm]
A	[−2; +2]	± 0.5
B	[−5; +5]	± 1.5
C	[−10; +10]	± 3.0

The simulated residual errors and noise, herein called the "residual interferogram noise", are then added to the noise-free interferograms. Three sets of assumed 8778 Gaussian noise values with zero mean are generated for each of the 1000 pixels and bounded within [−2; +2] mm, [−5; +5] and [−10; +10] mm, which correspond to standard deviations of approximately ± 0.5 mm, ± 1.5 mm and ± 3.0 mm, respectively (Table 3). Specifically, for each pixel, we first generate 8778 random samples of a Gaussian distribution with a zero mean and a standard deviation of one. These are subsequently rescaled so that their ranges lie exactly within the bounds set in Table 3. We acknowledge that the residual errors and noise in real SAR data may not be Gaussian with zero mean because they originate from a variety of sources (e.g., DEM error, orbital ramp, atmospheric delay, etc). However, we would only ever be able to postulate the actual statistical distribution of real InSAR data errors, so instead make the simple assumption of Gaussian zero mean for our simulations.

The simulated residual interferogram noise is generated in such a way that longer baseline lengths are assigned with noise of higher magnitude. Additionally, they have different ranges with the temporal baselines being from ~0.03 year to ~3.97 years, whilst the perpendicular baselines being between −376 meters and 400 meters. Therefore, they are first "normalized" by dividing all elements by the maximum value:

$$\begin{aligned} norm\_btemp_i &= \frac{btemp_i}{max(btemp)} \\ norm\_bperp_i &= \frac{abs(bperp_i)}{max\,[abs(bperp)]} \end{aligned} \tag{9}$$

where $norm\_btemp_i$ and $norm\_bperp_i$ are the "normalized" temporal and perpendicular baselines of the i^{th} interferogram, respectively which correspond to their values before "normalization" *btemp* and *bperp*, *abs* (.) and *max*(.) indicate the absolute and maximum values, respectively.

By this "normalization", the normalized temporal and perpendicular baselines will have ranges between ~0 and 1. The normalized baseline lengths of all interferograms are then computed with the i^{th} interferogram being:

$$norm\_bsln_i = \sqrt{norm\_btemp_i^2 + norm\_bperp_i^2} \tag{10}$$

The normalized baseline lengths computed from Eq. (10) are then used to assign the residual interferogram noise. Specifically, for each pixel with corresponding noise set of 8778 samples, the noise is assigned to interferograms by a way that an interferogram with a longer normalized baseline length will be assigned with noise of larger magnitude. We acknowledge that the influences of temporal and perpendicular baselines on interferometric noise are different. While the influence of perpendicular baselines can be quantified via their relationship with DEM error (e.g., Lee et al., 2012), the influence of temporal baselines is more sophisticated, which is dependent on the change of atmosphere and target environment over time (Zebker et al., 1997; Zebker and Villasenor, 1992). Here, for the sake of simplicity, we assume the two types of baseline are equal in terms of their weights in calculating normalized baselines using Eq. (10).

Table 4
List of networks tested in this study based on various temporal baseline thresholds. The perpendicular baseline threshold is set fixed at 200 m (Fig. 1).

Temporal baseline threshold [days]	Number of interferograms
22	263
33	376
44	498
55	621
66	745
77	863
88	986

5. Disruptive influences of residual noise and network configuration

In order to assess the influence of residual noise and small baseline network configuration on SBAS-derived land deformation rates, various interferogram networks were formed through the use of different thresholds for the temporal baselines. Here, for the sake of simplicity initially, we restrict the perpendicular baseline length to 200 m and only vary the temporal baseline. Table 4 shows the temporal baseline thresholds that are applied with the resulting number of interferograms.

We apply the SBAS approach to subsets of our simulated noisy interferograms (Table 4) using the GIAnT software package (Agram et al., 2013; Agram et al., 2012). GIAnT incorporates most of the SBAS-based data processing approaches mentioned in the Introduction, including the "traditional" SBAS (e.g., Berardino et al., 2002; Cavalié et al., 2007; Schmidt and Bürgmann, 2003; Usai, 2003), the new SBAS (NSBAS) (Doin et al., 2011; López-Quiroz et al., 2009), and the Multiscale InSAR Time-Series (MInTS) (Hetland et al., 2012); cf. Table 1. Time series of deformation relative to the first-acquired SAR image time for each of the 1000 test pixels are generated assuming that there is no deformation in the first acquisition. Both unweighted linear regression and unweighted LS are then applied to those SBAS time series in order to compute SBAS-derived linear rates and annual sinusoids, which are then compared with our simulated parameters listed in Table 2. The RMS of the difference between simulated deformation time series (the "true" signal) and SBAS-derived deformation time series is also computed in order to test dependence on the number of interferograms chosen.

5.1. Influences on simulated linear signals

We first examine a signal where Eq. (8) is adopted solely with the linear rate components of −2 mm/yr, −20 mm/yr and −100 mm/yr (Table 2). Fig. 2 shows results from different combinations of simulated deformation rates and residual interferogram error and noise. Here, the assumed simulated linear rates are considered as the "true" rates to which the SBAS-derived rates are compared and the differences between them are herein termed the "errors in rate determination". The SBAS rates are derived by fitting a linear regression to the corresponding deformation time series, then the errors in rate determination are calculated. The errors are shown in Fig. 2, and are the same in both magnitude and sign among all three simulated linear rate cases from Table 2. Generally, the larger simulated residual interferogram noise (i.e., [−10; +10] mm vs. [−5; +5] mm vs. [−2; +2] mm) leads to larger errors in the rate determination (cf. blue, green and black plotlines in Fig. 2), whereas an increase in the number of chosen interferograms (by choosing a larger temporal baseline threshold) can reduce this error.

Additionally, while their trends are in an agreement for the cases of larger signal rates (i.e., −20 mm/yr and −100 mm/yr, Fig. 2, middle and right), contradictory trends exist in the cases of small deformation (i.e., −2 mm/year, Fig. 2, left), particularly when networks of fewer interferograms are used together with higher residual noise of [−5; +5] mm and [−10; +10] mm. Importantly, the SBAS-derived deformation trends are affected by not only the magnitude of noise, but also its relation to the signal size (see Fig. 2, left), thus low SNR is more likely to result in incorrect or even contradictory trend estimates. In essence, small deformation rates in the presence of proportionally large noise may lead to spurious results, which become exacerbated in the presence of significant data gaps.

The "errors in rate determination" are next compared for the networks listed in Table 4 and shown in Fig. 3 for four example pixels. Within a specific network and pixel, the retrieved rate errors are identical when the same residual noise is applied regardless of the signal rates. In other words, if a specific network chosen from Table 4 with corresponding interferogram noise set is applied, then its error in rate determination will not depend on the magnitude of simulated rate (cf. blue, orange and yellow bars in Fig. 3). This is attributable to SBAS using the LS principle (Schmidt and Bürgmann, 2003) or the SVD method (Berardino et al., 2002). The results computed from applying the LS principle depend on redundant interferograms, together with residual interferogram error and noise that in turn depends on the configuration of the network (Berardino et al., 2002). The SBAS network configuration is specified by the design matrix $\boldsymbol{A}$ as per Eq. (1). Both the LS principle and SVD method result in the same InSAR-derived rates, except that the latter can cope with disconnected subsets of interferogram networks, whereas the former cannot (Berardino et al., 2002; Gong et al., 2016). Consequently, the same error in rate determination will result if the same residual noise is applied to a network regardless of the deformation rate.

5.2. Influences on non-linear signals

We next examine the signal combining both a linear trend and sinusoidal annual terms. As mentioned in Section 4, we apply pairs of signal parameters of linear rate plus annual amplitude, which are −2 mm/yr plus 2 mm, −20 mm/yr plus 5 mm, and −100 mm/yr plus 10 mm (Eq. (8)) as listed in Table 2. Via this simulation, we will test the influence of non-linearity of signal on unweighted linear fit rates, which are derived by fitting a linear regression to the SBAS-derived deformation time series.

Like the previous test of a linear signal only, the simulated deformation time series is generated by first applying Eq. (8) for all 1000 pixels prior to forming 8778 noise-free interferograms and applying simulated residual interferogram noise. The networks shown in Table 4 are then applied in sequence to select corresponding stacks of interferograms, which are then utilized with the SBAS method. Both the unweighted linear fit and unweighted LS methods are subsequently adopted to derive linear rates and annual amplitudes. Additionally, the RMSs between simulated and SBAS-derived time series are calculated.

Fig. 4 shows unweighted linear-fit rates computed using the linear rates from Table 2 and the simulated noise in Table 3. These results in Fig. 4 reflect the influence of signal non-linearity on linear-fit rates through biases in rate errors, particularly the case of large annual amplitudes, i.e., strongly non-linear, (cf. Fig. 4 between red lines and coloured polylines). This is due to the inappropriate functional model used here to derive the linear rates, i.e., linear regression, which is applied to linear plus annual simulated signal.

The simulated signal function is known (Eq. (8)), so we adopt this for estimating both rates and annual amplitudes utilizing unweighted LS (Fig. 5). The results indicate similar behavior as that in the case of solely linear signals (cf. Fig. 5 (top) with Fig. 2) and those with biases removed (cf. Fig. 5 (top) and Fig. 4). Again, this is attributable to the SBAS method in which the results computed depend on the configuration of the network and residual interferogram noise but not the deformation rate. Also, it is due to the more appropriate functional model used to obtain the linear rates where the influence of the signal non-linearity cancel out. It is therefore an important warning that a suitable function should be utilized to calculate linear rates in case the

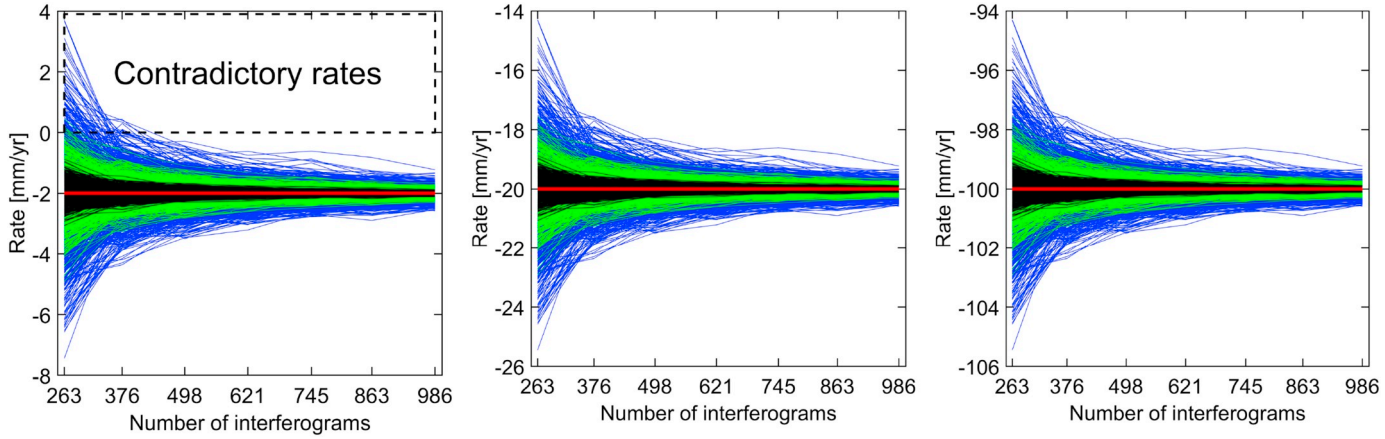

Fig. 2. Comparison of rates computed by unweighted linear fit from combinations of different deformation signals. From left to right are simulated linear rate cases 1 to 3 (Table 2) contaminated by simulated residual interferogram noise. Black, green and blue polylines are SBAS derived rates computed from simulated data with simulated noise cases A to C, respectively (Table 3). Red horizontal lines represent the simulated rates. The black dashed box in the left panel is used to contrast between positive and negative rates that indicates contradictory trends. (For interpretation of the references to colour in this figure legend, the reader is referred to the web version of this article.)

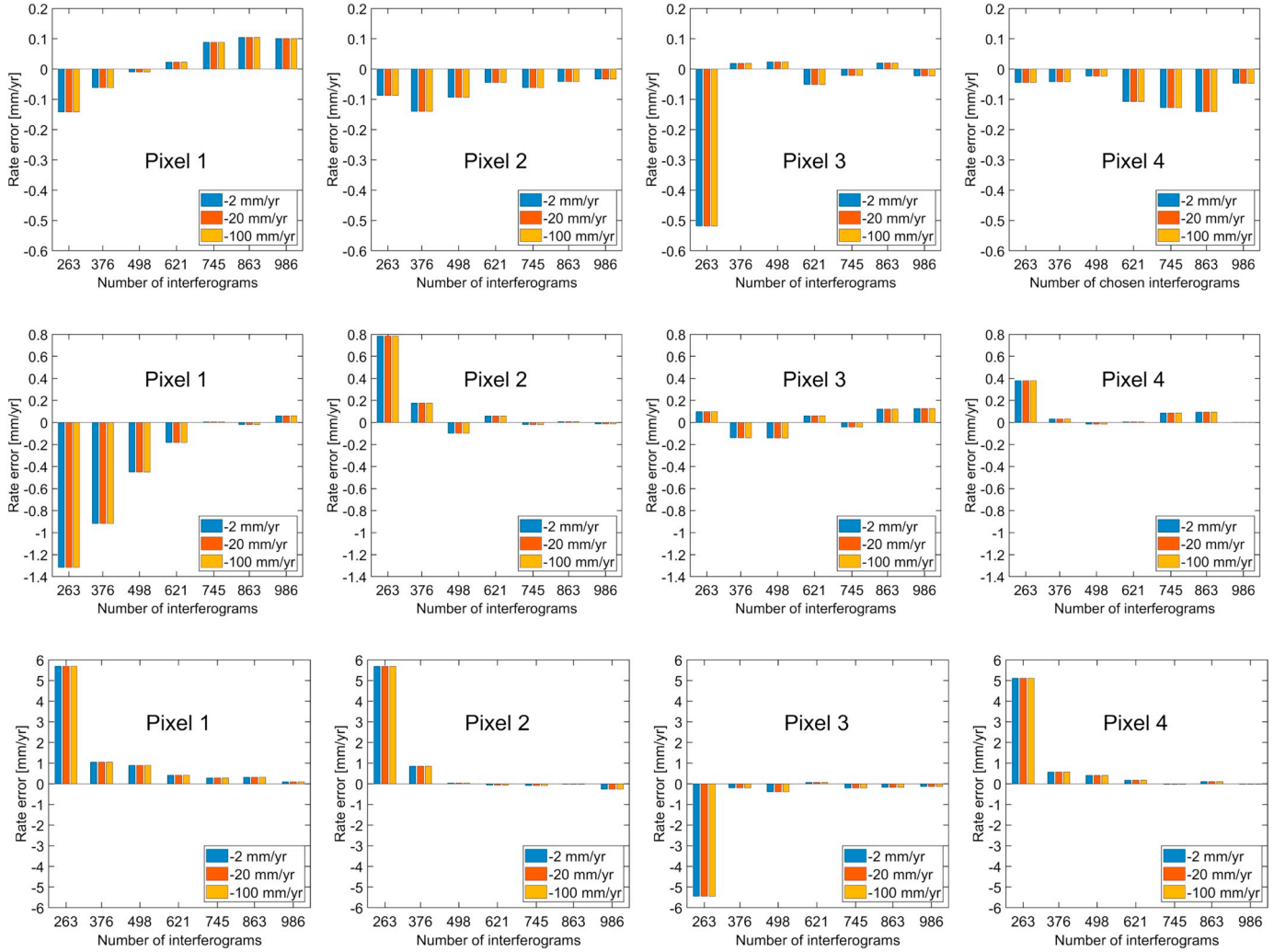

Fig. 3. Comparison of rate errors computed from different networks for four example pixels. The top, center and bottom rows correspond to simulated noise cases A, B and C (Table 3). Note the different scale on the y-axis for each noise case. (For interpretation of the references to colour in this figure legend, the reader is referred to the web version of this article.)

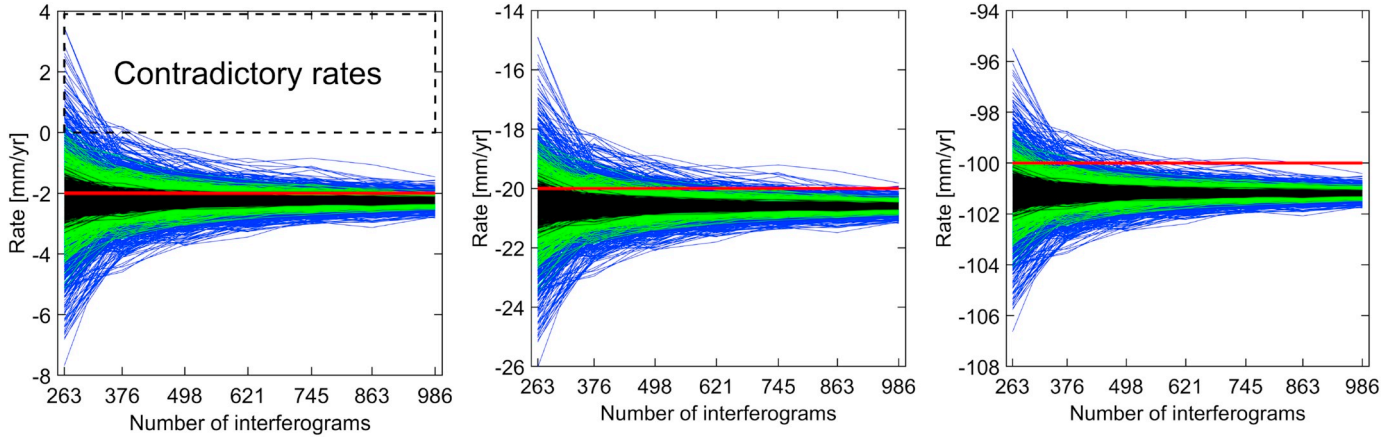

Fig. 4. Comparison of unweighted linear-fit rates from linear plus annual signals. From left to right are simulated signal cases 1 to 3 (Table 2) contaminated by various simulated residual interferogram noise. Black, green and blue polylines indicate the results computed from simulated data with noise cases A, B and C (Table 3). Red horizontal lines represent the simulated rates. The black dashed box in the left panel used to contrast between positive and negative rates that indicates contradictory trends in some cases. (For interpretation of the references to colour in this figure legend, the reader is referred to the web version of this article.)

Earth's surface experiences non-linear deformation, particularly in strongly non-linear cases.

In the case of applying LS estimation with an appropriate function, not only the linear rate, but also its accompanying parameters, e.g., the annual amplitude in this study, will be obtained. This is shown in Fig. 5 (bottom), where the computed annual amplitudes indicate that more interferograms in the SBAS network result in more accurate LS estimation of the annual amplitude. In addition, the errors in those computed parameters are dependent on the SBAS network configuration and residual interferogram noise, but not the signal magnitude.

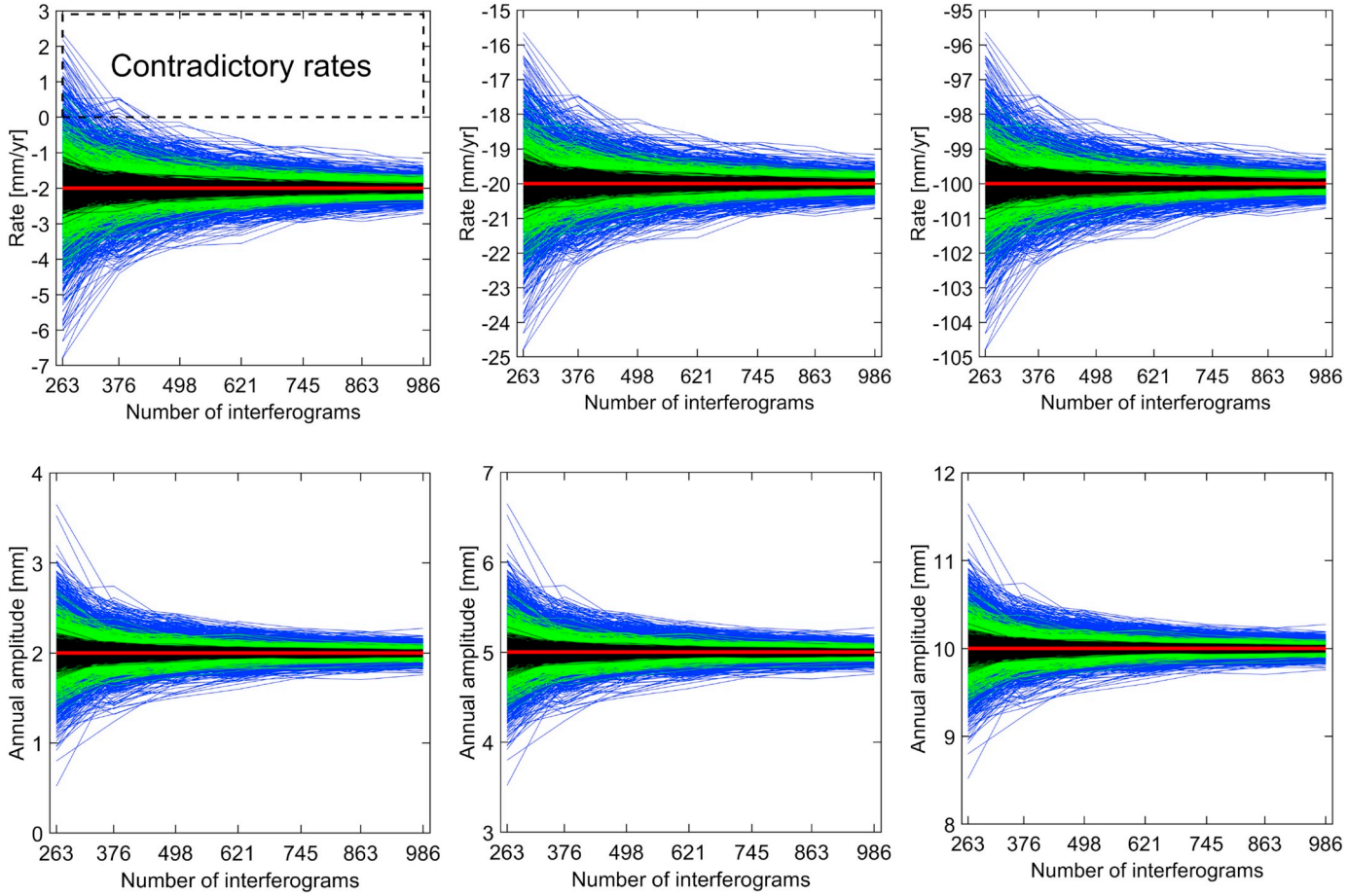

Fig. 5. Comparison of unweighted LS rates (top panel) and annual amplitudes (bottom panel) computed from linear plus annual signals. From left to right correspond to simulated signal cases 1 to 3 (Table 2) contaminated by various simulated residual interferogram noise. Black, green and blue polylines indicate the results computed from simulated data with noise cases A, B and C (Table 3). Red horizontal lines represent the simulated rates or annual amplitudes. The black dashed box in the top-left panel used to contrast between positive and negative rates that indicates contradictory trends in some cases. (For interpretation of the references to colour in this figure legend, the reader is referred to the web version of this article.)

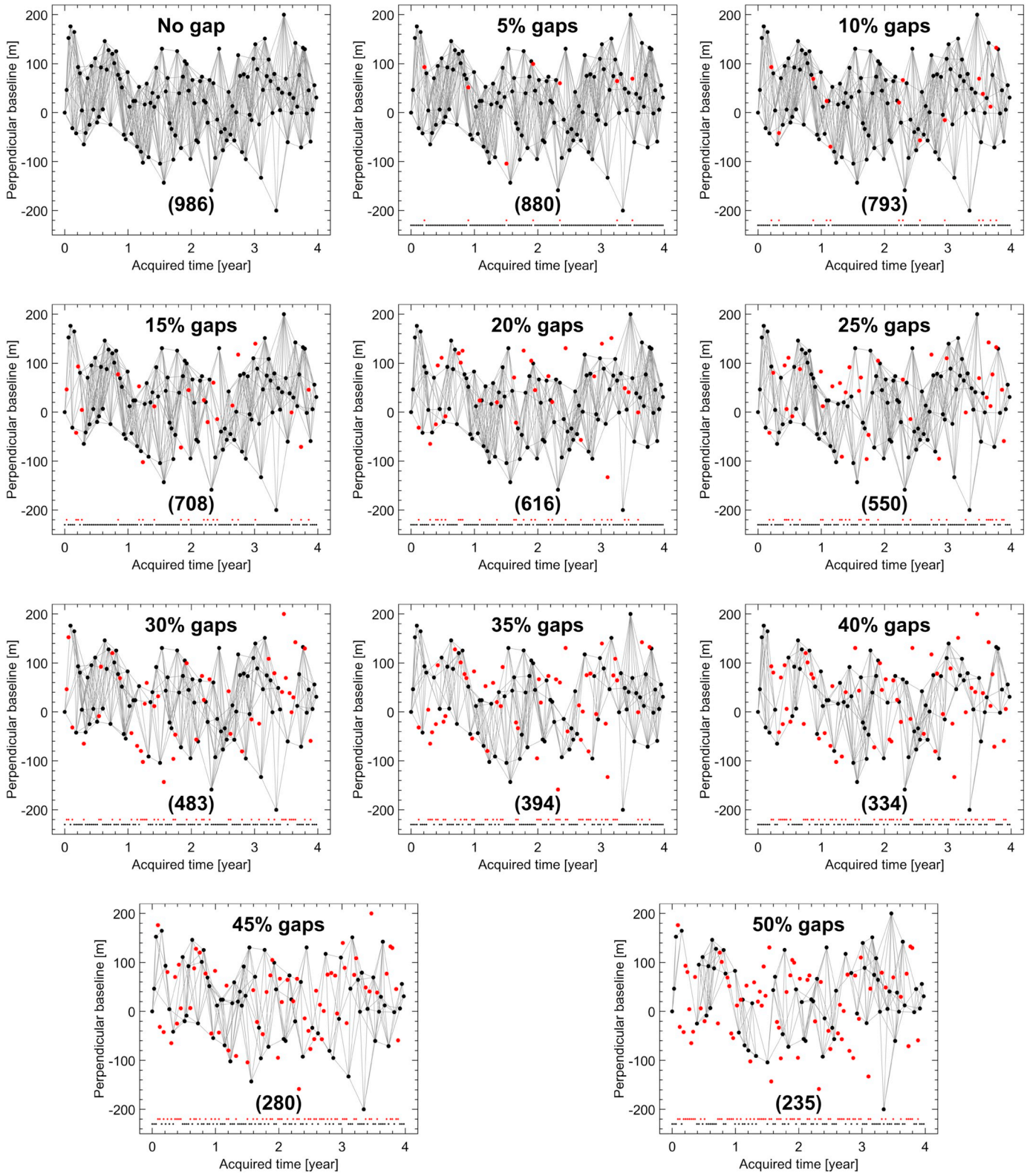

Fig. 6. Comparison of the interferogram network gaps in percentage. Gray lines indicate InSAR interferograms connecting images denoted by black dots. Red dots indicate missing images (i.e., gaps). The number under each network refers to the number of interferograms. (For interpretation of the references to colour in this figure legend, the reader is referred to the web version of this article.)

6. Influence of data gaps on SBAS-derived rates

In this Section, we study the influence of SAR data gaps on SBAS-retrieved rates. This is motivated by the likelihood of irregular temporal sampling of SAR data due to scheduling or other technical issues, such as decorrelation during winter snow cover. We now conduct simulations with a network of 986 interferograms formed by applying a temporal baseline threshold of 88 days (~ 3 months, Table 4), with two

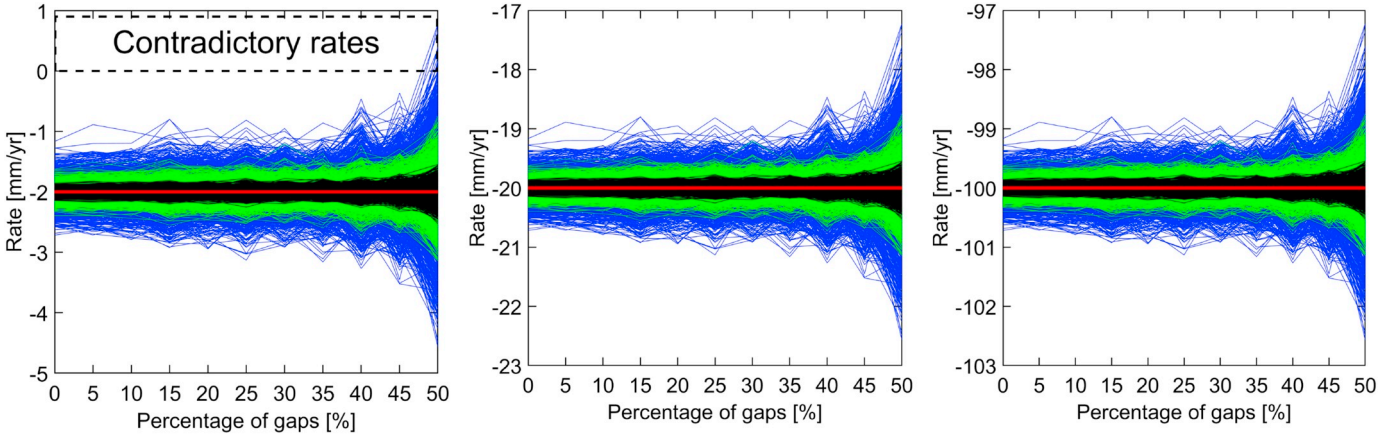

Fig. 7. Comparison of unweighted LS rates computed from linear plus annual signals between the interferogram network of no gaps and those with randomly chosen gaps of various percentages. From left to right correspond to simulated signal cases 1 to 3 (Table 2) contaminated by various simulated residual interferogram noise. Black, green and blue polylines indicate the results computed from simulated data with noise cases A, B and C (Table 3). Red horizontal lines represent the simulated rates. The black dashed box in the left panel used to contrast between positive and negative rates that indicates contradictory trends in some cases. (For interpretation of the references to colour in this figure legend, the reader is referred to the web version of this article.)

scenarios of data gaps. In the first scenario, missing images are due to technical and/or scheduling issues, which are considered random, and, in the second scenario, missing images are chosen in the northern winter season which are assumed to have low coherence due to extreme weather.

6.1. Random data gaps

In this Sub-section, we assume there are, in turn, 5%, 10%, …, 50% of acquisitions missing from our simulated time series. First, missing images are randomly chosen. Interferograms having connections with those missing images are subsequently identified and eliminated from the original list of 986 interferograms. Fig. 6 compares the network without gaps and those corresponding to various amount of gaps in percentage from 5% to 50% with an increment of 5%.

Here, we use the same linear plus annual signals as those used in Section 5.2 according to simulated signal cases shown in Table 2. For each network shown in Fig. 6, the SBAS approach in GIAnT is applied to all 1000 pixels in which the deformation time series at each pixel is derived. The unweighted LS is then applied to calculate the deformation rates and the RMSs of the difference between simulated and SBAS-derived time series are then calculated.

Fig. 7 compares SBAS-derived unweighted LS rates between the SBAS network with no gaps and those of different percentages of data gaps. Fig. 8 shows the corresponding RMSs of the difference between simulated and SBAS-derived deformation time series. These RMSs are the same for all three cases of linear plus annual signal (Table 2). Fig. 7 and Fig. 8 confirm that data gaps have an effect on the retrieved rates and RMSs with a noticeably larger influence in cases of higher gap percentages, particularly the 50% case. Contradictory trends are obtained for some pixels the case of large residual interferogram noise and low magnitude rates (Fig. 7, left). This is likely caused by a weak SBAS network configuration (see Fig. 6 with the 50% gaps case).

The influence of random data gaps on the errors in rate determination and the RMSs of the difference between simulated and SBAS-derived deformation time series is caused by a reduction in the number of interferograms when the percentage of gaps increases. However, a reduction in interferograms in the SBAS network can be caused by random data gaps (Figs. 7 and 8) or by changing the temporal baseline thresholds (as shown in Section 5). We compare errors resulting from fewer interferograms in a SBAS network due to (1) random gaps and (2) temporal baseline thresholds in Fig. 9 (cf. blue and green polylines). This demonstrates the role of the network configuration, where a network may have the same number of interferograms, but will have

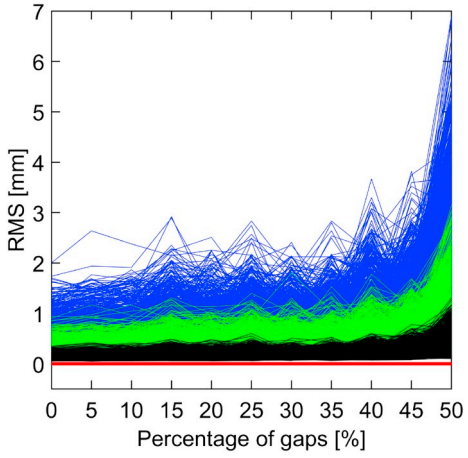

Fig. 8. Comparison of the RMSs of the difference between simulated and SBAS-derived deformation time series of all pixels between the SBAS interferogram network of no gap and those with random gaps. Black, green and blue polylines indicate the results computed from simulated data with noise cases A, B and C (Table 3). (For interpretation of the references to colour in this figure legend, the reader is referred to the web version of this article.)

higher errors depending on which interferograms are selected.

The random gap scenario results in more redundant interferograms, making the network more robust, especially in the case of noisier time series (Fig. 9, right plots). Therefore, in this case of randomly selected data gaps, mixed interferograms covering both short and long time spans makes the network more robust in recovering the deformation signal compared to the case of no gaps in which only short-time interferograms are chosen, which are limited by the threshold.

6.2. "Winter" data gaps

The previous test on data gaps in Section 6.1 is based on the fact that SAR data is missing sometime due to technical and/or scheduling issues, which we consider random. There is an alternative situation where there may be "user-defined" data gaps in which data missing is due to, e.g., very low coherence caused, for instance, by snow cover. We term this situation "winter data gaps" where all images acquired in the winter season (we use December to February for the Northern Hemisphere) are removed (Fig. 10).

The results of this simulation experiment are shown in Fig. 11. We

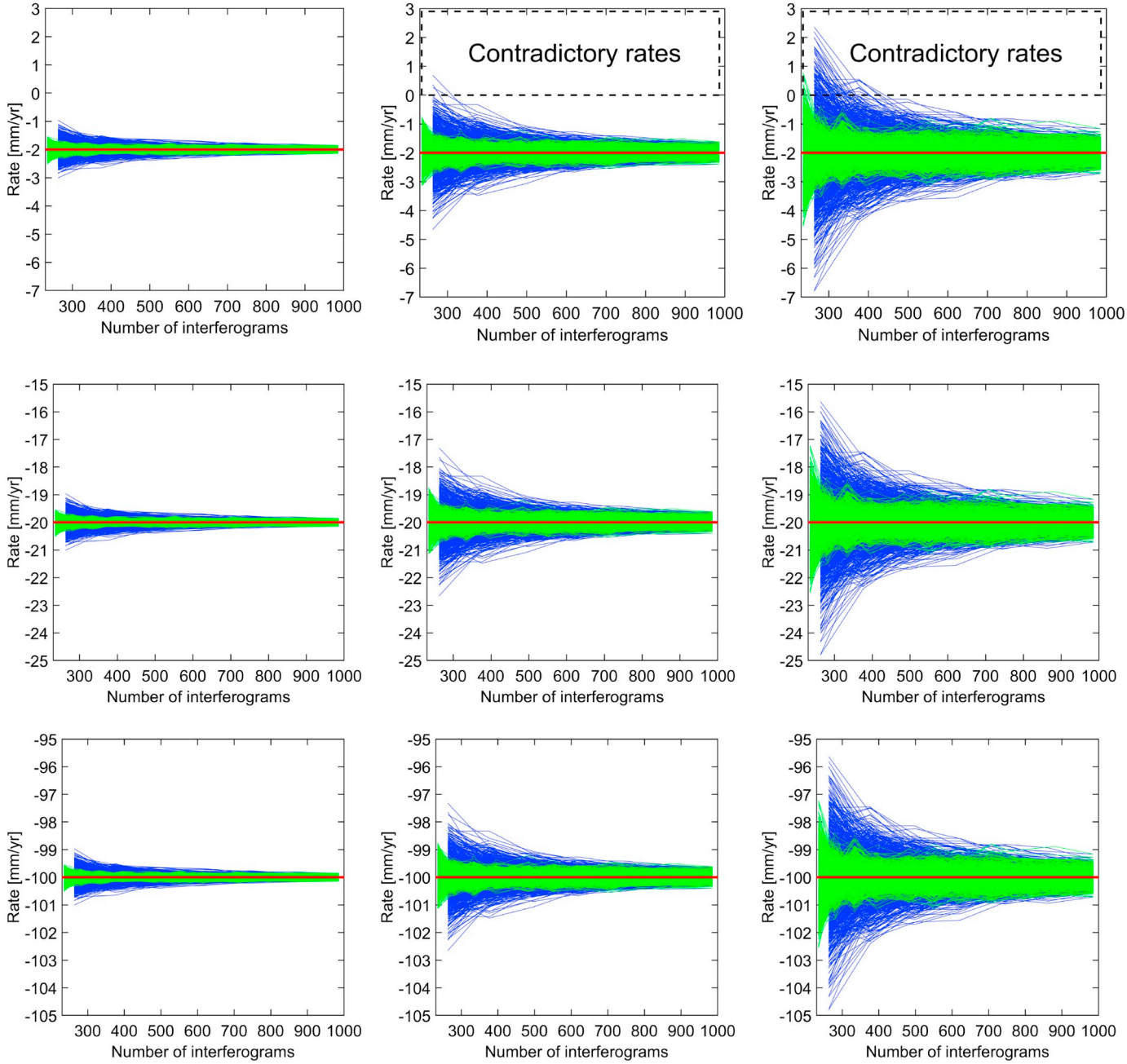

Fig. 9. The influence of the change in number of interferograms chosen by various temporal baseline thresholds (blue) and due to random data gaps (green) on SBAS-derived unweighted LS rates. From top to bottom: simulated signal cases 1, 2 and 3 (Table 2). From left to right: residual interferogram noise cases A to C (Table 3). Black dashed boxes in the top panel used to contrast between positive and negative rates that indicates contradictory trends in some cases. (For interpretation of the references to colour in this figure legend, the reader is referred to the web version of this article.)

compute unweighted LS rates and RMSs of the difference between simulated and SBAS-derived deformation time series for networks with no gaps, random data gaps and "winter data gaps", with the latter two having the same number of images. To avoid a disconnection in the SBAS network, we apply a network of 1340 interferograms formed by applying a temporal baseline threshold of 121 days (~4 months), instead of ~3 months as in Section 6.1, and a perpendicular baseline threshold of 200 m.

Fig. 11 compares unweighted LS rates for each network with RMSs between simulated and SBAS-derived deformation time series shown in Fig. 12. Fig. 10 shows the number of missing images is the same between the two cases of data gaps, which is 34 out of 133, and, though the missing images are selected differently, the number of interferograms linking the remaining images are nearly the same; 750 for random gaps and 744 winter gaps. However, the influence of these two different data gap cases are distinct with the "winter" gaps having a larger influence, as confirmed by both retrieved rates in Fig. 11 and RMSs in Fig. 12.

This is caused by the strength of the network configuration, which is more robust with interferograms at regular intervals in the random gaps network but with "blocks" of gaps in the "winter" case, leading to a less robust network (cf. Fig. 10 (middle) and (right)). This alerts users that, in addition to the effect of fewer interferograms and gap percentages, the strength of network configuration is another factor influencing the SBAS results, in which one should try to design a SBAS network that does not contain long gaps in the time series.

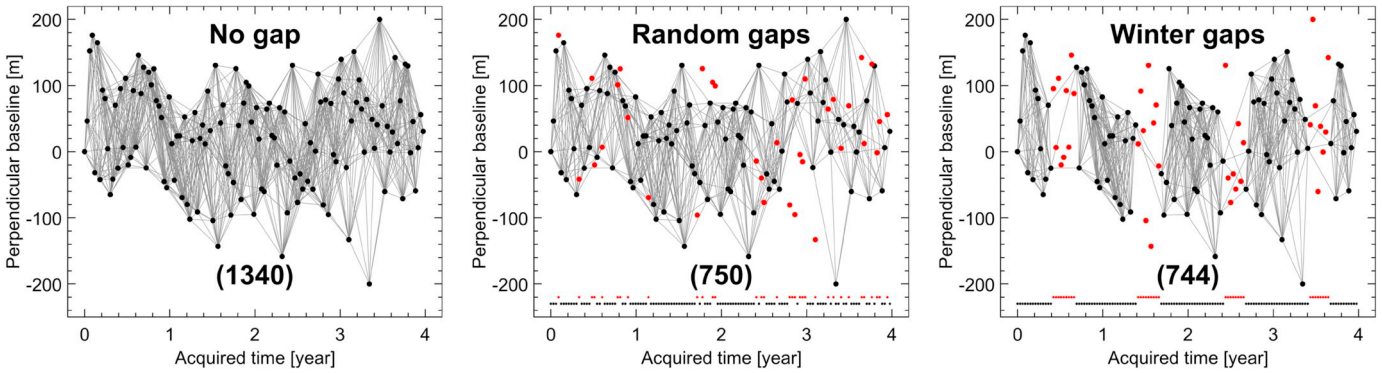

Fig. 10. Interferogram networks without (left) and with (middle, right) missing images. The number of missing images is 34 out of 133 corresponding to about 25%, which are selected randomly (middle) and in the northern winter season (right). The networks are formed using a temporal baseline threshold of ~4 months and a perpendicular baseline threshold of 200 m. Gray lines indicate interferograms, with images denoted by black dots. Red dots indicate missing images (i.e., gaps). The number under each network refers to the number of interferograms. (For interpretation of the references to colour in this figure legend, the reader is referred to the web version of this article.)

7. Optimal design of InSAR SBAS networks using redundancy numbers

As has been demonstrated in Section 5, a spurious deformation trend (uplift instead of simulated subsidence) can be retrieved by applying SBAS, particularly in the case of small deformation in relation to large residual error and noise (i.e., a low SNR). By using more interferograms, the rate error can be decreased as the redundancy in the network is increased. However, an increased number of interferograms will also result in a higher computational burden. In this Section, "optimal" network design from geodesy is adopted for InSAR based on redundancy or *r*-numbers (Section 3). The motivation here is to investigate the relation between RMSs of the difference between simulated and SBAS-derived deformation time series, number of selected interferograms and the redundancy number.

Here, we test interferogram networks determined by combinations of temporal baseline thresholds, from one month to four years long, with a one-month increment, and perpendicular baseline thresholds of 100 m, 200 m and 300 m. As a result, 144 networks are formed with the minimum and maximum number of interferograms being 251 and 8778, respectively. Eq. (6) is then applied to each of these networks to compute the *r*-numbers.

The reliability matrix $\boldsymbol{R}$ computed from Eq. (6) contains the *r*-numbers located on its diagonal (r_i). The objective of this optimization

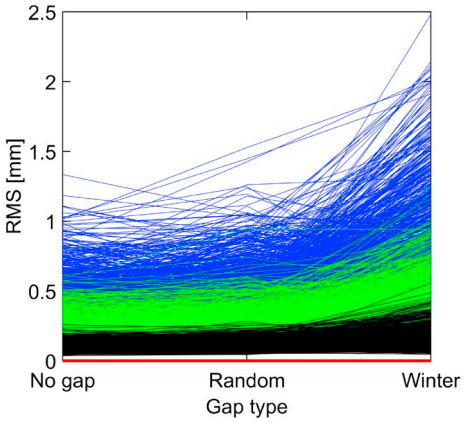

Fig. 12. Comparison of the RMSs of the difference between simulated and SBAS-derived deformation time series for all pixels between the interferogram networks of no gaps and those with randomly chosen gaps and "winter" gaps corresponding to ~25% missing images. Black, green and blue polylines indicate the results computed from simulated data with noise cases A, B and C (Table 3). (For interpretation of the references to colour in this figure legend, the reader is referred to the web version of this article.)

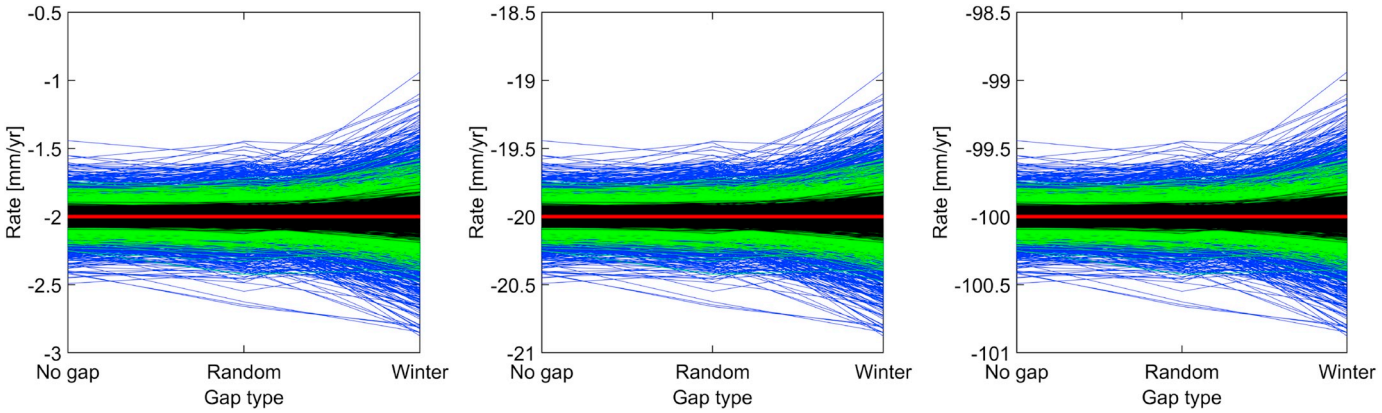

Fig. 11. Comparison of unweighted LS rates computed from linear plus annual signals according to interferogram networks with no gaps, random gaps and "winter" gaps. The networks adopt a temporal baseline threshold of ~4 months and a perpendicular baseline threshold of 200 m. From left to right are simulated signal cases 1 to 3 (Table 2). Black, green and blue polylines indicate the results computed from simulated data with noise cases A, B, and C (Table 3). Red horizontal lines represent the simulated rate. (For interpretation of the references to colour in this figure legend, the reader is referred to the web version of this article.)

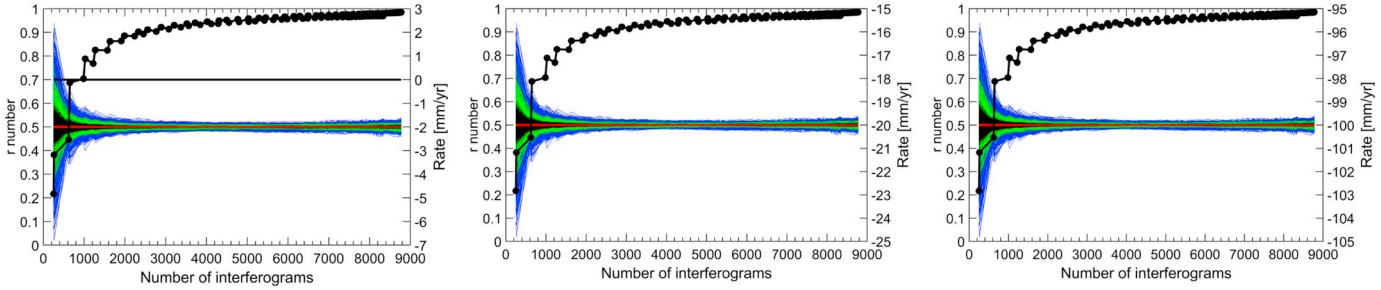

Fig. 13. The dependence of the *r*-numbers and SBAS-derived unweighted LS rates for 1000 pixels on the number of chosen interferograms with various linear plus annual signals. From left to right are simulated signal cases 1 to 3 (Table 2). Black, green and blue polylines show the results for noise cases A, B and C (Table 3). Red horizontal lines represent the simulated rates. (For interpretation of the references to colour in this figure legend, the reader is referred to the web version of this article.)

is to maximize these *r*-numbers by using their minimum value to represent the reliability of a network so that the *r*-numbers of all measurements in that network are larger or equal to this minimum value. The *r*-number of a network is thus defined as:

$$r = min(r_i) \tag{11}$$

The SBAS method was then applied to derive deformation time series for all 1000 pixels, again using GIAnT. We examine the same linear plus annual signals as those tested in Sections 5.1 and 6 (Table 2). The unweighted LS method is then utilized to derive SBAS-retrieved rates and the RMSs of the difference between simulated and SBAS-derived deformation time series are calculated.

The dependence of computed *r*-numbers and SBAS-retrieved annual rates on the number of selected interferograms are shown in Fig. 13, where the change in SBAS-derived unweighted LS rates presents the same patterns among the three cases (Table 2) of simulated signals. Furthermore, the higher the *r*-number, the closer the agreement between simulated and SBAS-retrieved rates. The two rates are, in particular, nearly identical when the *r*-numbers are greater than ~0.9.

The dependence of the RMSs of the difference between simulated and SBAS-retrieved deformation time series on the number of chosen interferograms are shown in Fig. 14 (left) for all three cases of simulated noise (Table 3). The *r*-number increases as the number of interferograms increases, constrained by temporal baseline thresholds, and a reduction in the RMSs. The RMSs decrease from a small *r*-number until ~0.8, after which the change becomes negligible.

We then apply 1/10 RMS as a trade-off value to identify the "optimal" *r*-number in which a network with a minimal number of interferograms selected and with all RMSs smaller than 1/10 noise range, which are 0.2 mm, 0.5 mm and 1.0 mm for the simulated residual interferogram noise ranges shown in Table 3. Recall that the RMSs are dependent on the SBAS network and residual interferogram noise but not signal magnitude (Fig. 3). Thus, Fig. 14 indicates an "optimal" *r*-number being ~0.86 for a SBAS network of 1911 interferograms, suggesting *r*-numbers between ~0.8 and ~0.9 to be a suitable range for the "optimal" design of SBAS networks.

The efficiency of the obtained "optimal" *r*-numbers are confirmed by not only the RMS trade-off, but also the computation time as shown in Fig. 14 (right), where the network of 1911 interferograms (for the "optimal" *r*-number) runs for less than four minutes compared to nearly 20 min for the largest network of 8778 interferograms. This shows efficiency in processing time for the SBAS inversion step only. In reality, SBAS data processing with a full workflow, which comprises additional steps of interferogram formation and error correction (e.g., DEM, orbital and atmospheric errors) the time difference between processing all 8778 interferograms and the optimal 1911 interferograms can be substantial. Additionally, this "optimal" design of SBAS networks keeps the number of interferograms to a minimum, which limits the disk storage space required.

Fig. 15 shows an example of the SBAS-derived deformation time series of a pixel compared with a simulated linear plus annual signal of −2 mm/yr plus 2 mm (i.e., the simulated signal case 1 in Table 2) according to selected cases of computed *r*-number of ~0.2, ~0.8 and ~0.9. The results of applying residual noise cases A, B, and C (Table 3) are shown in Fig. 15. In all cases, the results corresponding to the computed *r*-numbers of ~0.8 and ~0.9 show close agreement with the simulated signal. In contrast, however, large differences between simulated and SBAS-derived deformation time series are shown in the case when the *r*-number is ~0.2 (251 interferograms), particularly in the case of large residual interferogram noise (i.e., bounded within [−10; +10] mm) where the difference in both its trend (i.e., deformation or uplift) and magnitude is shown (cf. Fig. 15 (right) between

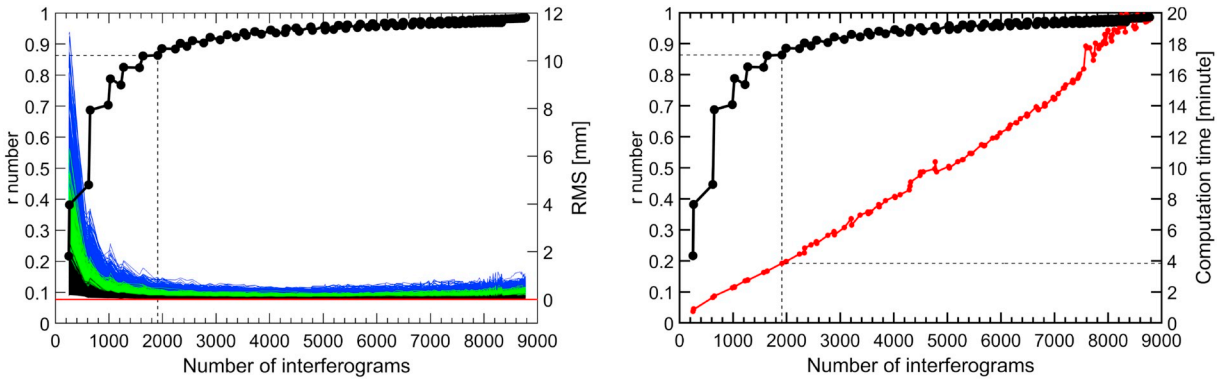

Fig. 14. (left): Comparison of the change in the *r*-numbers and the RMSs of the difference between simulated and SBAS-derived deformation time series. Black, green and blue polylines indicate the results computed from simulated data with noise cases A, B and C (Table 3). Dashed lines indicate the "optimal" *r*-numbers corresponding to the networks with smallest amount of interferograms chosen with all RMSs being smaller than the chosen trade-off values of 1/10 of the residual interferogram noise (Table 3). (right): Comparison of the change in the *r*-numbers according to SBAS network interferogram numbers and computation time.

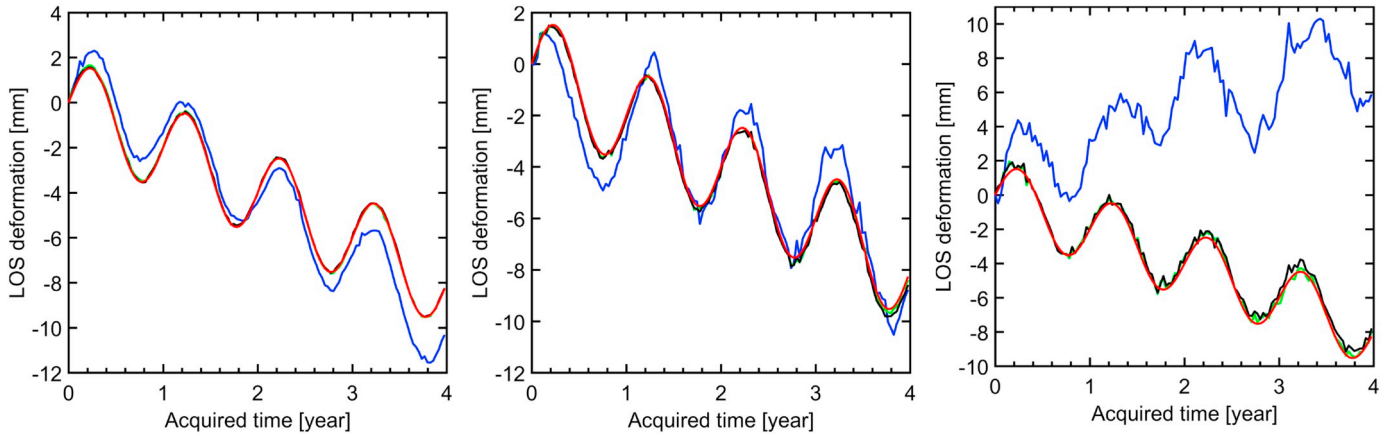

Fig. 15. An example of simulated and SBAS-derived deformation time series of simulated signal of linear rate plus annual amplitude of −2 mm/yr plus 2 mm (simulated signal case 1 in Table 2) contaminated by residual interferogram noise cases A (left), B (middle) and C (right) as listed in Table 3. The results are computed from applying various SBAS interferogram networks corresponding to computed *r*-numbers of ~0.2 (251 interferograms, blue polylines), ~0.8 (1571 interferograms, green polylines), and ~0.9 (2330 interferograms, black polylines), respectively. Red polylines indicate the simulated deformation time series. The blue line in the right panel shows the extreme case where spurious uplift is indicated, whereas subsidence is simulated. (For interpretation of the references to colour in this figure legend, the reader is referred to the web version of this article.)

the blue and red polylines).

Fig. 15 shows that if the *r*-number is too small (< 0.2), spurious or even contradictory rates can result, as was shown similarly in Section 5. Therefore, caution must be exercised when using InSAR to detect small rates of deformation in the presence of large noise (low SNR). This is where the redundancy number may be of assistance in gauging the reliability of the estimated rates. This also shows that, though the reliability of a network is relevant to its ability to detect and resist against gross errors, in this specific case of InSAR SBAS networks, a good agreement between the *r*-numbers and errors in rate determination is present that is useful for "optimal" design of InSAR SBAS networks.

8. Conclusions

This study has used simulated Gaussian noise with zero mean applied to interferograms computed from simulated linear and annual sinusoidal trends to demonstrate the effects of interferometric noise on InSAR SBAS derived deformation. This extends to how different SBAS network configurations may influence the estimated deformation rates. Different simulated rates are tested (Table 2), including the addition of annual periodic amplitudes so as to represent a range of real SAR data. A Monte Carlo simulation with 1000 pixels for each scenario was adopted. Firstly, we investigated the linear deformation signal, finding that the SBAS linear-fit deformation trends were sensitive to both the magnitude of interferometric noise and signal size. The unweighted linear-fit rate error was the same in both magnitude and size for all rates if the same residual noise is applied to a given network. The trend may become contradictory for small magnitude deformation where, for example a − 2 mm/yr rate could be estimated from the SBAS least squares or SVD method as a spurious uplift. This contradictory result was shown when small temporal thresholds of 33 days or less were used, which resulted in a less robust SBAS network configuration with fewer interferograms.

When we tested the linear plus annual periodic signal with interferometric noise, the linear-fit rates were biased in the linear rate (from the 1000 pixels) compared to the simulated rate. Alternatively, when we estimated the rates using a more suitable periodic functional model, rather than just linear regression in the presence of non-linear terms, the estimated rates were not biased. This demonstrates the potential for errors to be introduced by using simple linear regression when non-linear deformation may also be occurring.

Because one of the strengths of the SBAS method is to provide redundant small interferogram baselines (in space and time), we simulated the effect of missing SAR acquisitions in the time series. We presumed that these gaps in the time series would be (1) random that may be due to satellite mission scheduling issues, or (2) blocks of missing interferograms over, for example, a northern winter with snow covered ground that causes decorrelation. Our simulation results indicate that "winter" gaps causes a larger error in the estimated rates and in the RMSs of the differences between simulated and SBAS-derived deformation time series than for random gaps resulting from missed acquisitions. However, the RMS for both random gaps and no gaps were mostly 1 mm, while the winter gaps RMS was generally < 2 mm, suggesting that random gaps have little influence. This is highlighted when random gaps are compared to temporal threshold limits, showing that for the same number of interferograms, limiting temporal thresholds can cause errors of up to 6 mm/yr with noisy simulated data, compared to ~3 mm/yr for random gaps when using similar interferogram numbers. This suggests that it is the configuration of the SBAS network that is more important, to the point that caution should be exercised when reducing the temporal baseline to increase the coherence of the interferograms, because the trade-off may be a geometrically weak SBAS network that is vulnerable to incorrect rate estimation in the presence of noisy data and non-linear deformation.

We ran an additional simulation investigating whether redundancy numbers from geodetic theory could be adapted to design an optimal SBAS network. The simulation results suggest that *r*-values between ~0.8 and ~ 0.9 indicated a robust SBAS network design, and that including more interferograms beyond this provided little improvement in the accuracy of the rate estimation.

We conclude finally that SBAS network design can be critical to correctly estimate deformation rates, particularly in the case of low signal to noise ratios, and where the deformation may be non-linear. Notably, we found an alarming artifact in a couple of different simulation scenarios, where uplift was indicated by the SBAS rather than true simulated subsidence. It therefore appears that the configuration (network design) is more important than simply the number of interferograms used, which is important given any limits on computing resources. For this reason, we recommend the use of redundancy numbers to help optimize SBAS network design.

Declaration of Compeing Interest

The authors declare that they have no known competing financial interests or personal relationships that could have appeared to influence the work reported in this paper.

Credit author statement

All authors participated in devising the simulations, writing, editing and revising the manuscript. Some additional aspects were based on the anonymous reviewers' comments, which we have placed in the Acknowledgements. Luyen K. Bui processed and analyzed the data simulations.

Acknowledgements

Luyen Bui is supported by the Australia Awards Scholarships (AAS) provided for postgraduate study. Will Featherstone's InSAR projects are supported financially by Australian Research Council linkage project LP140100155, Landgate (the Western Australian geodetic agency), the Western Australian Department of Water, and Curtin University. We would like to thank California Institute of Technology (Caltech) for providing the source code of the Generic InSAR Analysis Toolbox (GIAnT). Finally, we thank the editor and two anonymous reviewers for their thorough and constructive handling of our manuscript, particularly the advice to consider non-linear signals and “winter” gaps.

References

Amelung, F., Galloway, D.L., Bell, J.W., Zebker, H.A., Laczniak, R.J., 1999. Sensing the ups and downs of Las Vegas: InSAR reveals structural control of land subsidence and aquifer-system deformation. Geology 27 (6), 483–486. https://doi.org/10.1130/0091-7613(1999)027<0483:STUADO>2.3.CO;2.

Agram, P.S., Jolivet, R., Simons, M., 2012. GIAnT - the Generic InSAR Analysis Toolbox - User Manual. Retrieved 09 June 2018, from. http://earthdef.caltech.edu/attachments/download/15/GIAnT_doc.pdf.

Agram, P.S., Jolivet, R., Riel, B., Lin, Y.N., Simons, M., Hetland, E., Doin, M.P., Lasserre, C., 2013. New radar interferometric time series analysis toolbox released. Eos, Transactions, American Geophysical Union 94 (7), 69–70. https://doi.org/10.1002/2013EO070001.

Amiri-Simkooei, A.R., 2001. Comparison of reliability and geometrical strength criteria in geodetic networks. J. Geod. 75 (4), 231–233. https://doi.org/10.1007/s001900100170.

Amiri-Simkooei, A.R., 2004. A new method for second order design of geodetic networks: aiming at high reliability. Surv. Rev. 37 (293), 552–560. https://doi.org/10.1179/sre.2004.37.293.552.

Amiri-Simkooei, A.R., Asgari, J., Zangeneh-Nejad, F., Zaminpardaz, S., 2012. Basic concepts of optimization and design of geodetic networks. J. Surv. Eng. 138 (4), 172–183. https://doi.org/10.1061/(ASCE)SU.1943-5428.0000081.

Baarda, W., 1968. A testing procedure for use in geodetic networks. In: Publication on Geodesy, New Series. 2 *Netherlands Geodetic Commission*, Delft Number 5.

Baldi, P., Casula, G., Cenni, N., Loddo, F., Pesci, A., 2009. GPS-based monitoring of land subsidence in the Po plain (northern Italy). Earth Planet. Sci. Lett. 288 (1–2), 204–212. https://doi.org/10.1016/j.epsl.2009.09.023.

Berardino, P., Fornaro, G., Lanari, R., Sansosti, E., 2002. A new algorithm for surface deformation monitoring based on small baseline differential SAR interferograms. IEEE Trans. Geosci. Remote Sens. 40 (11), 2375–2383. https://doi.org/10.1109/TGRS.2002.803792.

Berné, J.L., Baselga, S., 2004. First-order design of geodetic networks using the simulated annealing method. J. Geod. 78 (1–2), 47–54. https://doi.org/10.1007/s00190-003-0365-y.

Biggs, J., Wright, T., Lu, Z., Parsons, B., 2007. Multi-interferogram method for measuring interseismic deformation: Denali fault, Alaska. Geophys. J. Int. 170 (3), 1165–1179. https://doi.org/10.1111/j.1365-246X.2007.03415.x.

Bock, Y., Wdowinski, S., Ferretti, A., Novali, F., Fumagalli, A., 2012. Recent subsidence of the Venice Lagoon from continuous GPS and interferometric synthetic aperture radar. Geochem. Geophys. Geosyst. 13 (3), Q03023. https://doi.org/10.1029/2011GC003976.

Bombrun, L., Gay, M., Trouvé, E., Vasile, G., Mars, J., 2009. DEM error retrieval by analyzing time series of differential interferograms. IEEE Geosci. Remote Sens. Lett. 6 (4), 830–834. Article 5226568. https://doi.org/10.1109/LGRS.2009.2026434.

Cavalié, O., Doin, M.P., Lasserre, C., Briole, P., 2007. Ground motion measurement in the Lake Mead area, Nevada, by differential synthetic aperture radar interferometry time series analysis: probing the lithosphere rheological structure. Journal of Geophysical Research: Solid Earth 112 (3), 1–18. Article B03403.. https://doi.org/10.1029/2006JB004344.

Cavalié, O., Lasserre, C., Doin, M.-P., Peltzer, G., Sun, J., Xu, X., Shen, Z.-K., 2008. Measurement of interseismic strain across the Haiyuan fault (Gansu, China), by InSAR. Earth Planet. Sci. Lett. 275 (3–4), 246–257. https://doi.org/10.1016/j.epsl.2008.07.057.

Cavalié, O., Pathier, E., Radiguet, M., Vergnolle, M., Cotte, N., Walpersdorf, A., Kostoglodov, V., Cotton, F., 2013. Slow slip event in the Mexican subduction zone: evidence of shallower slip in the Guerrero seismic gap for the 2006 event revealed by the joint inversion of InSAR and GPS data. Earth Planet. Sci. Lett. 367, 52–60. https://doi.org/10.1016/j.epsl.2013.02.020.

Chaussard, E., Wdowinski, S., Cabral-Cano, E., Amelung, F., 2014. Land subsidence in Central Mexico detected by ALOS InSAR time-series. Remote Sens. Environ. 140, 94–106. https://doi.org/10.1016/j.rse.2013.08.038.

Chen, M., Tomás, R., Li, Z., Motagh, M., Li, T., Hu, L., Gong, H., Li, X., Yu, J., Gong, X., 2016. Imaging land subsidence induced by groundwater extraction in Beijing (China) using satellite radar interferometry. Remote Sens. 8 (6). https://doi.org/10.3390/rs8060468. Article 468.

Crosetto, M., Monserrat, O., Cuevas-González, M., Devanthéry, N., Crippa, B., 2016. Persistent Scatterer interferometry: a review. ISPRS J. Photogramm. Remote Sens. 115, 78–89. https://doi.org/10.1016/j.isprsjprs.2015.10.011.

Davis, J.L., Wernicke, B.P., Tamisiea, M.E., 2012. On seasonal signals in geodetic time series. Journal of Geophysical Research: Solid Earth 117 (B1), B01403. https://doi.org/10.1029/2011JB008690.

Delacourt, C., Briole, P., Achache, J., 1998. Tropospheric corrections of SAR interferograms with strong topography. Application to Etna. Geophys. Res. Lett. 25 (15), 2849–2852. https://doi.org/10.1029/98GL02112.

Didova, O., Gunter, B., Riva, R., Klees, R., Roese-Koerner, L., 2016. An approach for estimating time-variable rates from geodetic time series. J. Geod. 90 (11), 1207–1221. https://doi.org/10.1007/s00190-016-0918-5.

Doin, M.P., Lasserre, C., Peltzer, G., Cavalié, O., Doubre, C., 2009. Corrections of stratified tropospheric delays in SAR interferometry: validation with global atmospheric models. J. Appl. Geophys. 69 (1), 35–50. https://doi.org/10.1016/j.jappgeo.2009.03.010.

Doin, M.P., Lodge, F., Guillaso, S., Jolivet, R., Lasserre, C., Ducret, G., Grandin, R., Pathier, E., Pinel, V., 2011. Presentation of the small baseline NSBAS processing chain on a case example: the Etna deformation monitoring from 2003 to 2010 using Envisat data. In: *ESA Fringe Symposium*, Frascati, Italy: ESA SP-697, pp. 3434–3437. https://earth.esa.int/documents/10174/1573056/Presentation_small_baseline_NSBAS_Etna_deformation_Envisat.pdf.

Dzurisin, D., Lisowski, M., Wicks, C.W., 2009. Continuing inflation at three sisters volcanic center, Central Oregon Cascade Range, USA, from GPS, leveling, and InSAR observations. Bull. Volcanol. 71 (10), 1091–1110. https://doi.org/10.1007/s00445-009-0296-4.

Elliott, J.R., Walters, R.J., England, P.C., Jackson, J.A., Li, Z., Parsons, B., 2010. Extension on the Tibetan plateau: recent normal faulting measured by InSAR and body wave seismology. Geophys. J. Int. 183 (2), 503–535. https://doi.org/10.1111/j.1365-246X.2010.04754.x.

Fattahi, H., Amelung, F., 2013. DEM error correction in InSAR time series. IEEE Trans. Geosci. Remote Sens. 51 (7), 4249–4259. Article 6423275. https://doi.org/10.1109/TGRS.2012.2227761.

Ferretti, A., Prati, C., Rocca, F., 2001. Permanent scatterers in SAR interferometry. IEEE Trans. Geosci. Remote Sens. 39 (1), 8–20. https://doi.org/10.1109/36.898661.

Furuya, M., Mueller, K., Wahr, J., 2007. Active salt tectonics in the Needles District, Canyonlands (Utah) as detected by interferometric synthetic aperture radar and point target analysis: 1992-2002. Journal of Geophysical Research: Solid Earth 112 (6). https://doi.org/10.1029/2006JB004302. B06418, Article B06418.

Gatelli, F., Guarnieri, A.M., Parizzi, F., Pasquali, P., Prati, C., Rocca, F., 1994. The wavenumber shift in SAR interferometry. IEEE Trans. Geosci. Remote Sens. 32 (4), 855–865. https://doi.org/10.1109/36.298013.

Goel, K., Adam, N., 2014. A distributed scatterer interferometry approach for precision monitoring of known surface deformation phenomena. IEEE Trans. Geosci. Remote Sens. 52 (9), 5454–5468. Article 6679273. https://doi.org/10.1109/TGRS.2013.2289370.

Gong, W., Thiele, A., Hinz, S., Meyer, F.J., Hooper, A., Agram, P.S., 2016. Comparison of small baseline interferometric SAR processors for estimating ground deformation. Remote Sens. 8 (4), 1–26. Article 330. https://doi.org/10.3390/rs8040330.

Grafarend, E.W., Sansò, F., 1985. Optimization and Design of Geodetic Networks. Springer-Verlag, Berlin Heidelberg New York Tokyo. https://doi.org/10.1007/978-3-642-70659-2.

Hetland, E.A., Musé, P., Simons, M., Lin, Y.N., Agram, P.S., DiCaprio, C.J., 2012. Multiscale InSAR time series (MInTS) analysis of surface deformation. Journal of Geophysical Research: Solid Earth 117 (B2), B02404. https://doi.org/10.1029/2011JB008731.

Hooper, A., 2008. A multi-temporal InSAR method incorporating both persistent scatterer and small baseline approaches. Geophys. Res. Lett. 35 (16), L16302 Article L16302. https://doi.org/10.1029/2008GL034654.

Hooper, A., Zebker, H.A., Segall, P., Kampes, B., 2004. A new method for measuring deformation on volcanoes and other natural terrains using InSAR persistent scatterers. Geophys. Res. Lett. 31 (23), L23611. https://doi.org/10.1029/2004GL021737.

Hooper, A., Segall, P., Zebker, H.A., 2007. Persistent scatterer interferometric synthetic aperture radar for crustal deformation analysis, with application to Volcán Alcedo, Galápagos. Journal of Geophysical Research: Solid Earth 112, B7. https://doi.org/10.1029/2006JB004763.

Hooper, A., Bekaert, D.P.S., Spaans, K., Arıkan, M., 2012. Recent advances in SAR interferometry time series analysis for measuring crustal deformation. Tectonophysics 514–517, 1–13. https://doi.org/10.1016/j.tecto.2011.10.013.

Jiang, L., Lin, H., Ma, J., Kong, B., Wang, Y., 2011. Potential of small-baseline SAR interferometry for monitoring land subsidence related to underground coal fires: Wuda (northern China) case study. Remote Sens. Environ. 115 (2), 257–268. https://doi.org/10.1016/j.rse.2010.08.008.

Jolivet, R., Grandin, R., Lasserre, C., Doin, M.P., Peltzer, G., 2011. Systematic InSAR tropospheric phase delay corrections from global meteorological reanalysis data. Geophys. Res. Lett. 38 (17), L17311 Article L17311. https://doi.org/10.1029/2011GL048757.

Jolivet, R., Lasserre, C., Doin, M.P., Guillaso, S., Peltzer, G., Dailu, R., Sun, J., Shen, Z.K.,

Xu, X., 2012. Shallow creep on the Haiyuan fault (Gansu, China) revealed by SAR interferometry. Journal of Geophysical Research: Solid Earth 117 (B6), B06401. https://doi.org/10.1029/2011JB008732.
Kim, J.W., Lu, Z., Jia, Y., Shum, C.K., 2015. Ground subsidence in Tucson, Arizona, monitored by time-series analysis using multi-sensor InSAR datasets from 1993 to 2011. ISPRS J. Photogramm. Remote Sens. 107, 126–141. https://doi.org/10.1016/j.isprsjprs.2015.03.013.
Koch, K.R., 1985. First order design: Optimization of the configuration of a network by introducing small position changes. In: Grafarend, E.W., Sansò, F. (Eds.), Optimization and Design of Geodetic Networks. Springer-Verlag, Berlin Heidelberg New York Tokyo, pp. 56–73. https://doi.org/10.1007/978-3-642-70659-2.
Kohlhase, A.O., Feigl, K.L., Massonnet, D., 2003. Applying differential InSAR to orbital dynamics: a new approach for estimating ERS trajectories. J. Geod. 77 (9), 493–502. https://doi.org/10.1007/s00190-003-0336-3.
Kroese, D.P., Brereton, T., Taimre, T., Botev, Z.I., 2014. Why the Monte Carlo method is so important today. Wiley Interdisciplinary Reviews: Computational Statistics 6 (6), 386–392. https://doi.org/10.1002/wics.1314.
Kuang, S., 1993. On optimal design of levelling networks. Australian Surveyor 38 (4), 257–273. https://doi.org/10.1080/00050326.1993.10438874.
Kuang, S., 1996. Geodetic network analysis and optimal design: concepts and applications. Ann Arbor Press, Chelsea, Michigan, pp. 368.
Lanari, R., Mora, O., Manunta, M., Mallorquí, J.J., Berardino, P., Sansosti, E., 2004. A small-baseline approach for investigating deformations on full-resolution differential SAR interferograms. IEEE Trans. Geosci. Remote Sens. 42 (7), 1377–1386. https://doi.org/10.1109/TGRS.2004.828196.
Lanari, R., Casu, F., Manzo, M., Zeni, G., Berardino, P., Manunta, M., Pepe, A., 2007. An overview of the small BAseline subset algorithm: a DInSAR technique for surface deformation analysis. Pure Appl. Geophys. 164 (4), 637–661. https://doi.org/10.1007/s00024-007-0192-9.
Lauknes, T.R., Zebker, H.A., Larsen, Y., 2011. InSAR deformation time series using an L1-norm small-baseline approach. IEEE Trans. Geosci. Remote Sens. 49 (1 PART 2), 536–546. Article 5512638. https://doi.org/10.1109/TGRS.2010.2051951.
Lee, C.W., Lu, Z., Jung, H.S., 2012. Simulation of time-series surface deformation to validate a multi-interferogram InSAR processing technique. Int. J. Remote Sens. 33 (22), 7075–7087. https://doi.org/10.1080/01431161.2012.700137.
Lin, Y.N.N., Simons, M., Hetland, E.A., Muse, P., Dicaprio, C., 2010. A multiscale approach to estimating topographically correlated propagation delays in radar interferograms. Geochem. Geophys. Geosyst. 11, 9), 1–17. Article Q09002. https://doi.org/10.1029/2010GC003228.
López-Quiroz, P., Doin, M.-P., Tupin, F., Briole, P., Nicolas, J.-M., 2009. Time series analysis of Mexico City subsidence constrained by radar interferometry. J. Appl. Geophys. 69 (1), 1–15. https://doi.org/10.1016/j.jappgeo.2009.02.006.
Lubitz, C., Motagh, M., Wetzel, H.U., Kaufmann, H., 2013. Remarkable urban uplift in Staufen im Breisgau, Germany: observations from terraSAR-X InSAR and leveling from 2008 to 2011. Remote Sens. 5 (6), 3082–3100. https://doi.org/10.3390/rs5063082.
Lundgren, P., Usai, S., Sansosti, E., Lanari, R., Tesauro, M., Fornaro, G., Berardino, P., 2001. Modeling surface deformation observed with synthetic aperture radar interferometry at Campi Flegrei caldera. Journal of Geophysical Research: Solid Earth *106* (B9), 19355–19366 Article 2001jb000194.
Mora, O., Mallorqui, J.J., Broquetas, A., 2003. Linear and nonlinear terrain deformation maps from a reduced set of interferometric SAR images. IEEE Trans. Geosci. Remote Sens. 41, 2243–2253. https://doi.org/10.1109/TGRS.2003.814657. 10 PART I.
Motagh, M., Djamour, Y., Walter, T.R., Wetzel, H.U., Zschau, J., Arabi, S., 2007. Land subsidence in Mashhad Valley, Northeast Iran: results from InSAR, levelling and GPS. Geophys. J. Int. 168 (2), 518–526. https://doi.org/10.1111/j.1365-246X.2006.03246.x.
Murray, K.D., Lohman, R.B., 2018. Short-lived pause in Central California subsidence after heavy winter precipitation of 2017. Sci. Adv. 4 (8). https://doi.org/10.1126/sciadv.aar8144. Article eaar8144.
Murray, K.D., Bekaert, D.P.S., Lohman, R.B., 2019. Tropospheric corrections for InSAR: statistical assessments and applications to the Central United States and Mexico. Remote Sens. Environ. 232https://doi.org/10.1016/j.rse.2019.111326. Article 111326.
Neely, W.R., Borsa, A.A., Silverii, F., 2020. GInSAR: a cGPS correction for enhanced InSAR time series. IEEE Trans. Geosci. Remote Sens. 58 (1), 136–146. Article 8839742. https://doi.org/10.1109/TGRS.2019.2934118.
Osmanoğlu, B., Dixon, T.H., Wdowinski, S., Cabral-Cano, E., Jiang, Y., 2011. Mexico City subsidence observed with persistent scatterer InSAR. Int. J. Appl. Earth Obs. Geoinf. 13 (1), 1–12. https://doi.org/10.1016/j.jag.2010.05.009.
Pepe, A., Ortiz, A.B., Lundgren, P.R., Rosen, P.A., Lanari, R., 2011. The Stripmap–ScanSAR SBAS Approach to Fill Gaps in Stripmap Deformation Time Series With ScanSAR Data. In: IEEE Transactions on Geoscience and Remote Sensing, https://doi.org/10.1109/TGRS.2011.2167979. 49(12 PART 1), 4788–4804, Article 6045335.
Schmidt, D.A., Bürgmann, R., 2003. Time-dependent land uplift and subsidence in the Santa Clara valley, California, from a large interferometric synthetic aperture radar data set. Journal of Geophysical Research: Solid Earth 108 (B9). https://doi.org/10.1029/2002JB002267.
Schmitt, G., 1985a. Review of network designs: Criteria, risk functions, design ordering. In: Grafarend, E.W., Sansò, F. (Eds.), Optimization and Design of Geodetic Networks. Springer-Verlag, Berlin Heidelberg New York Tokyo, pp. 6–10. https://doi.org/10.1007/978-3-642-70659-2.
Schmitt, G., 1985b. Third order design. In: Grafarend, E.W., Sansò, F. (Eds.), Optimization and Design of Geodetic Networks. Springer-Verlag, Berlin Heidelberg New York Tokyo, pp. 122–131. https://doi.org/10.1007/978-3-642-70659-2.
Shanker, P., Casu, F., Zebker, H.A., Lanari, R., 2011. Comparison of persistent scatterers and small baseline time-series InSAR results: a case study of the San Francisco bay area. IEEE Geosci. Remote Sens. Lett. 8 (4), 592–596. Article 5692806. https://doi.org/10.1109/LGRS.2010.2095829.
Short, N., Brisco, B., Couture, N., Pollard, W., Murnaghan, K., Budkewitsch, P., 2011. A comparison of TerraSAR-X, RADARSAT-2 and ALOS-PALSAR interferometry for monitoring permafrost environments, case study from Herschel Island, Canada. Remote Sens. Environ. 115 (12), 3491–3506. https://doi.org/10.1016/j.rse.2011.08.012.
Sowter, A., Bateson, L., Strange, P., Ambrose, K., Fifiksyafiudin, M., 2013. DInSAR estimation of land motion using intermittent coherence with application to the south derbyshire and leicestershire coalfields. Remote Sensing Letters 4 (10), 979–987. https://doi.org/10.1080/2150704X.2013.823673.
Teunissen, P.J.G., 1985. Zero order design: Generalized inverses, adjustment, the datum problem and S-transformations. In: Grafarend, E.W., Sansò, F. (Eds.), Optimization and Design of Geodetic Networks. Springer-Verlag, Berlin Heidelberg New York Tokyo, pp. 11–55. https://doi.org/10.1007/978-3-642-70659-2.
Tong, X., Sandwell, D.T., Smith-Konter, B., 2013. High-resolution interseismic velocity data along the San Andreas fault from GPS and InSAR. Journal of Geophysical Research: Solid Earth 118 (1), 369–389. https://doi.org/10.1029/2012JB009442.
Tymofyeyeva, E., Fialko, Y., 2015. Mitigation of atmospheric phase delays in InSAR data, with application to the eastern California shear zone. Journal of Geophysical Research: Solid Earth 120 (8), 5952–5963. https://doi.org/10.1002/2015JB011886.
Usai, S., 2003. A least squares database approach for SAR Interferometric data. In: *IEEE Transactions on Geoscience and Remote Sensing, 41*(4 PART I), pp. 753–760. https://doi.org/10.1109/TGRS.2003.810675.
Vaníček, P., Krakiwsky, E.J., 1986. Geodesy: The Concepts, 2nd ed. Elsevier Science Publisher, Amsterdam, The Netherlands.
Williams, S., Bock, Y., Fang, P., 1998. Integrated satellite interferometry: tropospheric noise, GPS estimates and implications for interferometric synthetic aperture radar products. Journal of Geophysical Research: Solid Earth 103 (B11), 27051–27067. Article 98jb02794. https://doi.org/10.1029/98jb02794.
Yague-Martinez, N., Prats-Iraola, P., Gonzalez, F.R., Brcic, R., Shau, R., Geudtner, D., Eineder, M., Bamler, R., 2016. Interferometric processing of Sentinel-1 TOPS data. IEEE Trans. Geosci. Remote Sens. 54 (4), 2220–2234. Article 7390052. https://doi.org/10.1109/TGRS.2015.2497902.
Yu, C., Penna, N.T., Li, Z., 2017. Generation of real-time mode high-resolution water vapor fields from GPS observations. J. Geophys. Res. 122 (3), 2008–2025. https://doi.org/10.1002/2016JD025753.
Yu, C., Li, Z., Penna, N.T., 2018a. Interferometric synthetic aperture radar atmospheric correction using a GPS-based iterative tropospheric decomposition model. Remote Sens. Environ. 204, 109–121. https://doi.org/10.1016/j.rse.2017.10.038.
Yu, C., Li, Z., Penna, N.T., Crippa, P., 2018b. Generic atmospheric correction model for Interferometric synthetic aperture radar observations. Journal of Geophysical Research: Solid Earth 123 (10), 9202–9222. https://doi.org/10.1029/2017JB015305.
Zebker, H.A., Villasenor, J., 1992. Decorrelation in interferometric radar echoes. IEEE Trans. Geosci. Remote Sens. 30 (5), 950–959. https://doi.org/10.1109/36.175330.
Zebker, H.A., Rosen, P.A., Hensley, S., 1997. Atmospheric effects in interferometric synthetic aperture radar surface deformation and topographic maps. Journal of Geophysical Research B: Solid Earth 102 (B4), 7547–7563 Article 96JB03804.